SECTION 1

RESEARCH IN PROGRESS

NUCLEAR REACTIONS -- EXPERIMENTAL

TWO-PROTON CORRELATION FUNCTIONS FOR ^{36}AR + ^{45}SC AT E/A=80 MEV

D.O. Handzy, M.A. Lisa, C.K. Gelbke, W. Bauer, F.C. Daffin, P. Dekowski, W.G. Gong, E. Gualtieri, S. Hannuschke, R. Lacey, T. Li, W.G. Lynch, C.M. Mader, G.F. Peaslee, T. Reposeur, S. Pratt, A.M. Vander Molen, G.D. Westfall, J. Yee, and S.J. Yennello

Two–proton correlation functions probe the space–time extent of the reaction zone created in energetic nucleus–nucleus collisions, because the magnitude of the nuclear and Coulomb final–state interactions, as well as antisymmetry effects, depend on the spatial separation of the two protons at the time of emission [1-6].

"Angle integrated" correlation functions (those with no explicit cut on $\psi = \cos^{-1}(\vec{P}\cdot\vec{q}/Pq)$, where $\vec{P}$ is the proton–pair total momentum and $\vec{q}$ is the proton–pair relative momentum) probe the volume of the phase–space distribution of emitted particles with little sensitivity to its shape [4,7]. Without independent knowledge of the size of the emitting system and the emission mechanism (surface versus volume emission), "angle–integrated" correlation functions cannot discriminate between smaller sources of longer lifetime and large sources of shorter lifetime.

This space–time ambiguity may be reduced by analyzing two–proton correlation functions with cuts on ψ [1,4,7–11]. Emission from a long–lived source leads to a phase space distribution elongated in the direction of $\vec{P}$, the total momentum of the proton pair in the rest frame of the emitting source. The magnitude of this elongation is of order $P\tau/2m$ where τ is the average time interval between the emissions of the detected particles. Two–proton correlation functions exhibit a directional sensitivity primarily due to an increased Pauli suppression in the nonelongated (transverse) direction. For long–lived sources, transverse correlation functions ($\vec{q}\perp\vec{P}$) are therefore suppressed at small q in comparison with longitudinal correlation functions ($\vec{q}\parallel\vec{P}$). Since the total momentum, $\vec{P}$, depends upon the rest frame of the source, but the relative momentum, $\vec{q}$, does not, the angle ψ, and hence the definition of the longitudinal and transverse cuts, depends on the rest frame of the emitting system. Care must therefore be taken to characterize the rest frame of the emitting source [9,10,11].

The solid and open points of Figure 1 show the longitudinal and transverse correlation functions measured for central ^{36}Ar + ^{45}Sc collisions at E/A=80 MeV, with the angle ψ is defined in the center–of–momentum frame of the colliding system [10]. The central cuts correspond to $b(E_t) \le 0.36$. The top and bottom panels of the figure shows the results for low–momentum (P_{lab}=400–600 MeV/c) and high–momentum (P_{lab}=700–1400 MeV/c) protons, respectively. For consistency with References [10,12,13], we define our cuts on the magnitude of the total momentum defined in the laboratory frame, but we will use *different* rest frames for the definition of the angle ψ. Significant differences between longitudinal and transverse correlation functions are observed for the emission of slow protons, P_{lab}=400–600 MeV/c, but not for the emission of the faster protons, P_{lab}=700–1400 MeV/c, likely reflecting decreasing emission time scales for emitted protons of higher energy.

The solid and dashed curves in Figure 1 show longitudinal and transverse two–proton correlation functions predicted by BUU calculations which incorporate the effects due to the finite resolution of the centrality filter using the impact–parameter probability distribution, $dP/d\hat{b}_{true}$ of reference [13]. The calculations reproduce the magnitude and the difference between longitudinal and transverse correlation functions rather well, slightly over predicting the peak height at q≈20 MeV/c for the high–momentum protons, P_{lab}=700–1400 MeV/c. (bottom panel). Differences between longitudinal and transverse correlation functions caused by lifetime expansion effects are best shown by defining the angle ψ in the rest frame of the emitting system [10]. In less well–defined situations, other directional dependencies

may exist which may not be revealed by our choice of cuts on ψ. It is therefore instructive to explore angular cuts on ψ, defined in different rest frames and compare them to predictions of the BUU model.

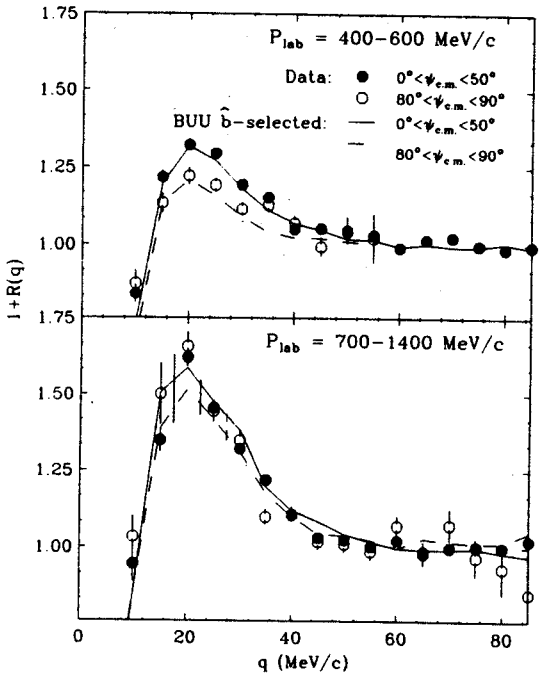

Figure 1: Solid and open points show longitudinal and transverse correlation functions measured for central collisions at the indicated momenta. The curves show BUU predictions employing impact–parameter selected calculations. The cuts on ψ were performed in the center–of–momentum frame.

The upper and lower panels of Figures 2 and 3 show longitudinal (solid points) and transverse (open points) correlation functions with cuts on ψ defined in the laboratory and projectile frames, respectively. The right and left panels show data for the low and high momentum cuts. In Figure 2, the data are compared with BUU predictions for the idealized case of $\hat{b}=0$. In Figure 3, they are compared to the more realistic impact–parameter gated calculations. For the low–momentum cut, P_{lab}=400–600 MeV/c, the differences between longitudinal and transverse correlation functions become insignificant when the cuts on ψ are defined in the laboratory frame (top, left panels of Figures 2 and 3) and in the projectile rest frame (bottom, left panels). These trends are rather well reproduced by the BUU calculations, using either the $\hat{b}=0$ (Figure 2) or realistic impact parameter weights (Figure 3). For the present reaction, the emission of low–energy protons at large angles ($\vartheta_{c.m.} \approx 90°$) appears to be rather well described by the BUU calculations, with little sensitivity to contributions from collisions at small, but nonzero, impact parameters. For the high momentum cut, P_{lab}=700–1400 MeV/c, no significant difference between measured longitudinal and transverse correlation functions is observed when the cuts on ψ are defined in the laboratory frame (right, top panels in Figures 2 and 3), but there is an indication for a small suppression of the transverse correlation function in the projectile rest frame (right, bottom panels). This difference, is, however, of marginal statistical significance. These trends are reasonably well reproduced by the BUU calculations using $\hat{b}=0$ (Figure 2) which do, however, over predict the magnitude of the peak at q ≈ 20 MeV/c. The BUU calculations employing the realistic impact–parameter distribution (Figure 3) predict a negligible difference between longitudinal and transverse correlation functions in the laboratory rest frame, in agreement with the experimental findings. In the projectile rest frame, however, these calculations predict a larger difference than observed

experimentally, possibly indicating that the calculations predict somewhat too large emission from projectile spectator matter than is observed experimentally.

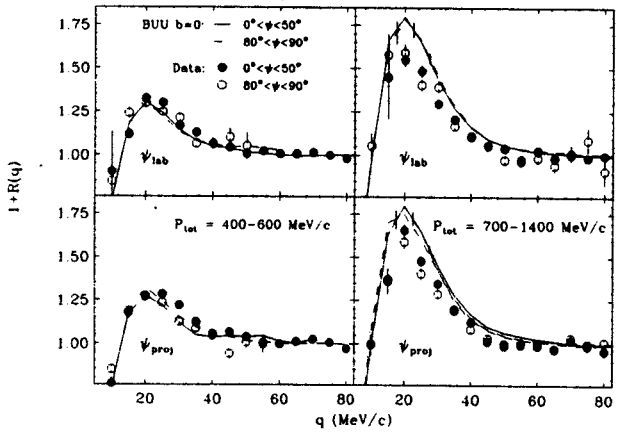

Figure 2: Longitudinal (solid points and curves) and transverse (open points and dashed curves) correlation functions constructed in the laboratory (top) and projectile (bottom) rest frames. Left and right panels show results for low– and high–momentum cuts, respectively. Points show data selected by the centrality cut $b(E_t) \leq 0.36$, and the curves show BUU predictions for $b = 0$.

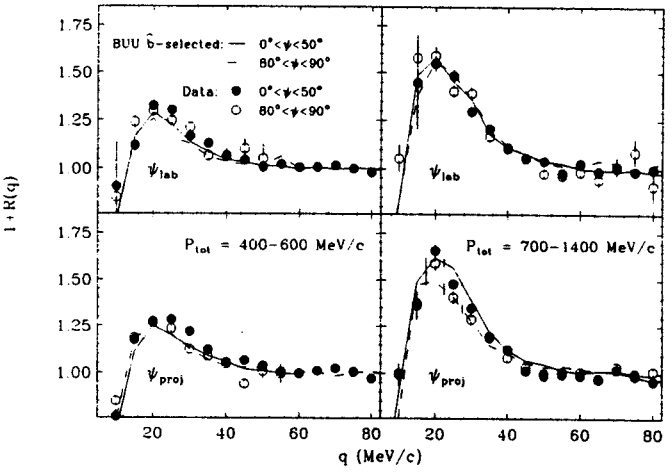

Figure 3.: Longitudinal (solid points and curves) and transverse (open points and dashed curves) correlation functions constructed in the laboratory (top) and projectile (bottom) rest frames. Left and right panels show results for low– and high–momentum cuts, respectively. Points show data selected by the centrality cut $b(E_t) \leq 0.36$, and the curves show BUU predictions employing the impact–parameter probability distribution of Reference 13.

In order to gain additional insight into the rest–frame dependence of longitudinal and transverse correlation functions predicted by BUU transport calculations, we plot in Figure 4 the relative split, $\langle \Delta R \rangle / \langle R \rangle$, between longitudinal and transverse correlation functions calculated for specific impact parameters, b=0, 3, and 6 fm, and for different rest frame velocities, $v_\psi = c\beta_\psi$ with respect to the laboratory frame. $\Delta R = R_{long} - R_{trans}$ is the difference between the longitudinal and transverse correlation functions evaluated in a given rest frame, R is the angle integrated correlation function which is independent of rest frame, and the $\langle\ \rangle$ denotes the average value over the interval $15\ \text{Mev/c} \leq q \leq 40\ \text{MeV/c}$. The top and bottom panels of Figure 4 show the values of $\langle \Delta R \rangle / \langle R \rangle$ predicted

for the cuts P_{lab}=400–600 MeV/c and P_{lab}=700–1400 MeV/c, respectively. For the low momentum cut, P_{lab}=400–600 MeV/c, the predictions for central collisions (b=0, solid circles) follows the trends of the data: the largest value of $\langle \Delta R \rangle / \langle R \rangle$ is predicted in the center–of–momentum of projectile and target, and very small differences are predicted for longitudinal and transverse cuts on ψ defined in the target (laboratory) or projectile rest frames. A qualitative interpretation of this observation was first given in Reference [10]. As the velocity of the y–frame (β_ψ) increases, the axis defined by $\vec{P}$ "rotates" through the spatial distribution of emitted nucleons. The relative difference between the longitudinal and transverse correlation functions, $\langle \Delta R \rangle / \langle R \rangle$, will be maximal when the axis is oriented along the distribution of emitted protons, which occurs when β_ψ assumes the value of the velocity of the rest frame of the emitting source.

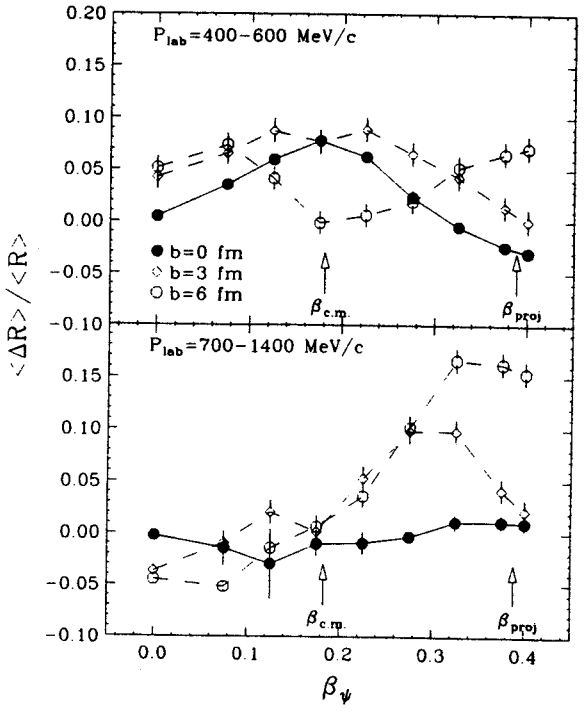

Figure 4: Relative difference, $\langle \Delta R \rangle / \langle R \rangle$, between longitudinal and transverse correlation functions as a function of the velocity β_ψ of the rest frame in which the directional ψ cuts are defined. Shown are BUU predictions for b=0 (solid circles), b=3 fm (open diamonds) and b=6 fm (open circles). Results for low– and high–momentum cuts are displayed in the upper and lower panels, respectively.

A very different behavior is predicted for a large (b=6 fm) impact parameter (open circles in Figure 4) for the low–momentum cut. For these glancing collisions, no observable differences are predicted in the center–of–momentum frame. In contrast, significant differences are predicted when the ψ cuts are defined in the target and projectile rest frames, consistent with the intuitive expectations that emission of midrapidity protons in peripheral collisions is due to a superposition of emission from target and projectile like sources. For the high–momentum cut, P_{lab}=700–1400 MeV/c, differences between longitudinal and transverse correlation functions are predicted to be negligible for central (b=0) collisions, independent of rest frame. These predictions follow the trends of the data. Fast particle emission in central collisions appears to occur on a fast time scale, and elongations of the phase–space distribution from finite lifetime effects becomes negligible. For larger impact parameters, however, $\langle \Delta R \rangle / \langle R \rangle$ is predicted to become large for rest–frame velocities close to the projectile velocity, indicating

that fast, forward–emitted particles in peripheral collisions are predicted to have substantially (if not predominant) contributions from the decay of projectile residues. Note, however, that the BUU predictions for energetic emission in peripheral collisions do not reproduce the data – see Reference [10]. Furthermore, for our peripheral cut, no statistically significant differences between longitudinal and transverse correlation functions were found in the target, projectile, nor in the center–of–momentum rest frames [10,14]. These findings corroborate that the details of proton emission in peripheral collisions are not well described by our calculations.

Overall, the observed differences between longitudinal and transverse correlation functions were reproduced rather well by the BUU calculations with some slight disagreement emerging for the emission of high–energy protons when the longitudinal and transverse correlation functions were viewed in the projectile frame. These discrepancies could well arise from small admixtures of peripheral collisions for which the BUU predictions are less reliable. Small additional theoretical uncertainties exist due to ambiguities in the criteria of when and where a particle is emitted. Finally, the discrepancies for modestly peripheral collisions may indicate that the present model is incomplete in its description of such collisions and that it may be deficient in its description of surface effects. If so, the utility of the BUU in its present formulation may be limited to the description of very central collisions.

References

1. S.E. Koonin, Phys. Lett. **70B**, 43 (1977).
2. D.H. Boal, and J.C. Shillock, Phys. Rev. C **33**, 549 (1986).
3. D. H. Boal, and H. DeGuise, Phys. Rev. Lett. **57**, 2901 (1986).
4. S. Pratt and M.B. Tsang, Phys. Rev. C **36**, 2390 (1987).
5. D. H. Boal, C.K. Gelbke, and B.K. Jennings, Rev. Mod. Phys. **62**, 553 (1990).
6. W. Bauer, C.K. Gelbke, and S. Pratt, Annu. Rev. Nucl. Part. Sci. **42**, 77 (1992).
7. W.G. Gong, W. Bauer, C.K. Gelbke, and S. Pratt, Phys. Rev. C **43**, 781 (1991).
8. T.C. Awes, R.L. Ferguson, F.E. Obenshain, F. Plasil, G.R. Young, S. Pratt, Z. Chen, C.K. Gelbke, W.G. Lynch, J. Pochadzalla, and H.M. Xu, Phys. Rev. Lett. **61**, 2665 (1988).
9. D. Goujdama, F. Guilbault, C. Lebrun, D. Ardouin, H. Dabrowski, S. Pratt, P. Lautridou, R. Boisgard, J. Québert, and A. Péghaire, Z Phys. A **339**, 293 (1991).
10. M.A. Lisa, C.K. Gelbke, W. Bauer, P. Dekowski, W.G. Gong, E. Gualtieri, S. Hannuschke, R. Lacey, T. Li, W.G. Lynch, C.M. Mader, G.F. Peaslee, T. Reposeur, S. Pratt, A.M. Vander Molen, G.D. Westfall, J. Yee, and S.J. Yennello, Phys, Rev. Lett **71**, 2863 (1993).
11. D. Rebreyend, F. Merchez, B. Norén, E. Andersen, M. Cronqvist, J.C. Gondrand, H.A. Gustafsson, B. Jäger, B. Jacoksson, B. Khelfaouli, S. Kox, A. Kristiansson, G. Lövhöiden, S. Mattson, T.F. Thorsteinsen, M. Westenius, and L. Westerberg, Phys. Rev. C **46**, 2387 (1992).
12. M.A. Lisa, C.K. Gelbke, W. Bauer, P. Dekowski, W.G. Gong, E. Gualtieri, S. Hannuschke, R. Lacey, T. Li, W.G. Lynch, C.M. Mader, G.F. Peaslee, T. Reposeur, S. Pratt, A.M. Vander Molen, G.D. Westfall, J. Yee, and S.J. Yennello, Phys, Rev. Lett **70**, 3709 (1993).
13. D.O. Handzy, M.A. Lisa, C.K. Gelbke, W. Bauer, F.C. Daffin, P. Dekowski, W.G. Gong, E. Gualtieri, S. Hannuschke, R. Lacey, T. Li, W.G. Lynch, C.M. Mader, G.F. Peaslee, T. Reposeur, S. Pratt, A.M. Vander Molen, G.D. Westfall, J. Yee, and S.J. Yennello, Phys. Rev. C **50**, 858 (1995).
14. M.A. Lisa, Ph.D. Thesis, Michigan State University, August, 1993.

PROBING TOROIDAL DENSITY DISTRIBUTIONS WITH TWO–PROTON CORRELATION FUNCTIONS?

D.O. Handzy, S.J. Gaff, W. Bauer, F.C. Daffin, C.K. Gelbke, and G.J. Kunde

Calculations with the BUU model predict that disk–shaped [1] or toroidal [2,3,4,5,6] configurations may be produced in central heavy–ion collisions. Different observables have been suggested to find a signature of a toroidal breakup [1,2,5,7,8], but no experimental evidence for the formation of tori as yet exists. The suggested observables were based on either intuitive arguments [1,2,5] or on schematic calculations [7,8] in which a multifragment disintegration of the torus was assumed. However, none of these suggestions was substantiated by dynamical calculations capable of exploring the space–time evolution of the reaction zone. A consistent dynamical treatment is possible for nucleon emission and for the calculation of two–proton correlation functions, using the Koonin–Pratt formalism and the actually phase–space distributions predicted by the BUU theory.

Our analysis concentrates on simulations of central ^{36}Ar + ^{45}Sc collisions at E/A=80 MeV, performed with very high statistics. As shown in refs. [6,9,10], measured impact–parameter–filtered correlation functions for this reaction were reproduced successfully by BUU calculations. These same calculations predict the formation of a toroidal density distributions. The data were, however, also reproduced by assuming emission from a spherical source of finite lifetime [10]. Hence, the agreement with BUU calculations could not be taken as evidence for the predicted toroidal shapes; see also [6]. The system is predicted to evolve into a toroidal configuration which is symmetric about the beam axis. In order to isolate effects due to the spatial configuration of the emitting source, we make stringent cuts on the directions of total and relative momenta, as shown in Figure 1.

We first cut on the orientation of the total momentum, $\vec{P}$, which is selected to lie within ±10° of the (x,y) plane. The relative momentum, $\vec{q}$, is then selected (within ±10°) along three directions: $\vec{q}_{par}$ is parallel to $\vec{P}$ and thus sensitive to the source dimension and its lifetime; $\vec{q}_{beam}$ and $\vec{q}_{perp}$ are perpendicular to $\vec{P}$ and thus insensitive to lifetime effects. $\vec{q}_{perp}$ lies in the (x,y) plane and is thus sensitive to the radius of the torus, while $\vec{q}_{beam}$ is parallel to the beam axis and is thus sensitive to the thickness of the torus.

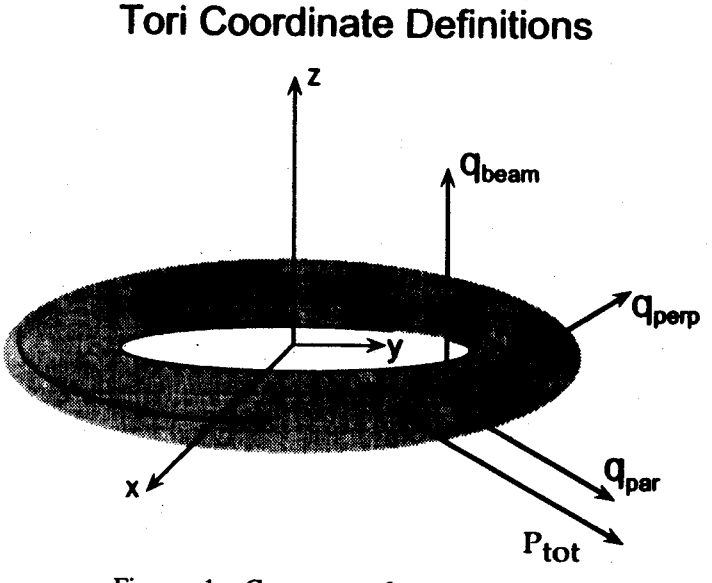

Figure 1: Geometry of torus and directions of applied cuts on q used in all our calculations.

The solid and dashed curves in Figure 2 show two–proton correlation functions calculated under the simplifying assumption of instantaneous emission from the volume of the toroidal density distribution at t=100 fm/c, as shown in the left hand panels of the insert. The momenta for this simulation were chosen isotropic in the center–of–mass frame, with a flat distribution for each Cartesian component ranging from –200 to 200 MeV/c. Statistical uncertainties of the calculations are indicated by the error bars. The correlation functions for $\vec{q}_{par}$ and $\vec{q}_{perp}$ (not shown in the figure) are practically degenerate, consistent with an instantaneous emission. The

correlation function for $\bar{q}_{beam}$ exhibits a strongly enhanced Pauli suppression, reflecting the shorter dimension of the torus (see figure 1). The open and solid points in figure 2 represent the results of calculations for instantaneous emission from a disk–shaped distribution obtained by uniformly filling the "hole" of the doughnut. (The torus and "disk" density distributions, which have approximately equal volumes, are compared in the right hand inserts of figure 2) The calculations for the two source geometries are very similar, indicating that our choice of directional cuts is not sensitive to the "hole" of the torus. It will be even more difficult, if not impossible, to differentiate between a disk and a torus with experimental correlation functions which average over the temporal evolution of the reaction zone over a finite window of impact–parameters. However, one may still hope to distinguish these "flat" shapes from spherically symmetric sources, even in a more realistic reaction scenario.

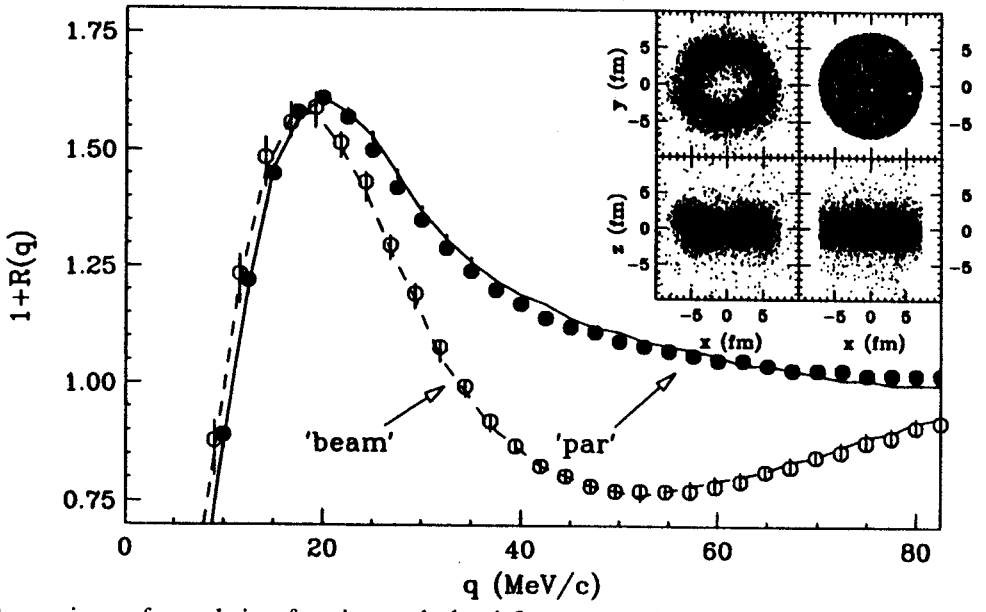

Figure 2: Comparison of correlation functions calculated for a zero–lifetime torus and disk. The assumed density distributions are depicted in the insert; torus on the left and disk on the right.

The degeneracy of $R(\bar{q}_{perp})$ and $R(\bar{q}_{par})$ is removed if emission occurs with a fixed lifetime. Specifically, we used the same toroidal spatial distribution employed previously, with an added exponential time dependence, $dN/dt \propto \exp(-t/\tau)$, with $\tau = 25$ fm/c.The magnitude of the peak of the correlation function at q ≈ 20 MeV/c is reduced, and the correlation functions are ordered approximately as $R(\bar{q}_{par}) \geq R(\bar{q}_{perp}) \geq R(\bar{q}_{beam})$, reflecting increased Pauli suppression due to smaller average particle separations along the respective directions.

Figure 2 suggest that two–proton correlation functions are well–suited to extract useful information about nonspherical sources of fixed geometries. This simplified scenario (of emission from a non–evolving source) serves only as an example. More realistic calculations will incorporate the dynamics of proton emission, and will include contributions from larger impact–parameter collisions, as described in the following section.

The insert of Figure 3 shows that the BUU transport model predicts, for strictly central collisions, that most of the protons are emitted before the torus is fully formed (at t ≈ 100 fm/c). This suggests that the differences between our directional cuts will be reduced, when employing the phase–space density distribution predicted by the BUU model, due to the substantial proton emission from the compact initial configurations (see Figure 1). Figure 3 shows that when employing the same cuts as defined in Figure 2 (with no restrictions on the magnitude of the total momentum) that the predicted differences are

significantly reduced. Although there is a clear difference between the correlation functions cut on $\bar{q}_{par}$ and $\bar{q}_{perp}$, indicative of the source lifetime, the toroidal signature (the difference between $\bar{q}_{perp}$ and $\bar{q}_{beam}$) is substantially diminished.

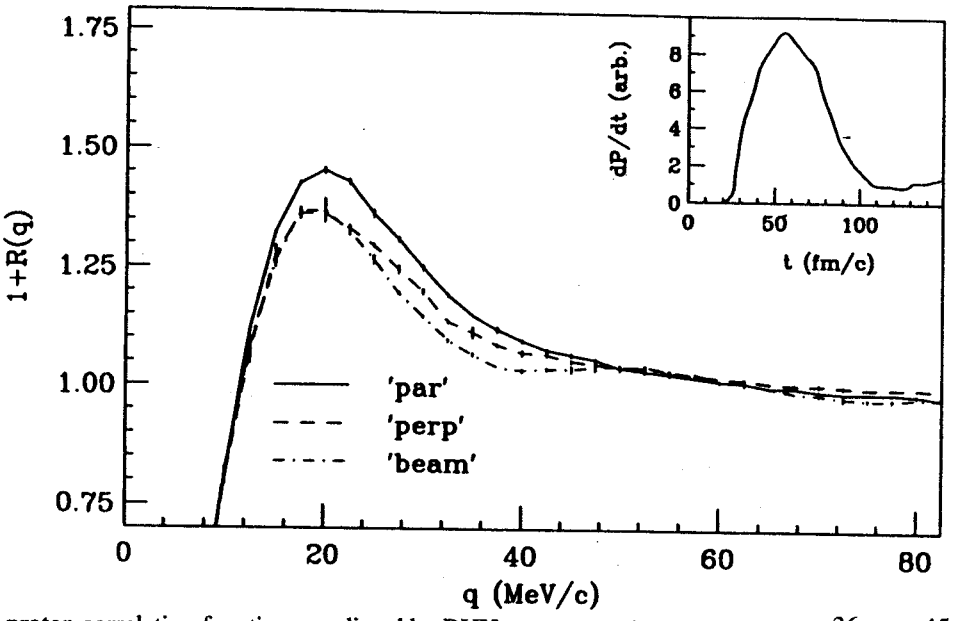

Figure 3: Two–proton correlation functions predicted by BUU transport calculations for b=0 ^{36}Ar + ^{45}Sc collisions at E/A=80 MeV. The insert shows the time dependence of proton emission.

Further complications arise when unavoidable contributions of nonzero impact parameters are taken into account. Toroidal shapes are predicted for small (nonzero) impact parameters, but their symmetry axes are tilted away from the beam axis. For impact parameters larger than about 3 fm, the residual system assumes stretched configurations leading to a binary exit channel, possibly accompanied by neck emission [11].

The impact parameter distribution used for the calculation of the two–proton correlation function for central collisions of ^{36}Ar + ^{45}Sc at E/A=80 MeV is shown in the insert of figure 4. With our choice of b_{max}=10 fm, this figure shows that the most likely impact–parameter for our central cut is about 3 fm, and that the distribution contains substantial contributions from larger impact–parameters.

Figure 4 illustrates the effects of impact–parameter averaging. The correlation functions shown in the figure were calculated using the fixed–axis directional cuts defined in Figure 2 and by employing the central–cut impact–parameter distribution shown in the insert. For tilted tori (i.e., for collisions with b > 0), the directional cut parallel to the beam axis no longer probes the smallest dimension of the residual system. As a consequence, the correlation function $R(\bar{q}_{beam})$ is less suppressed, and the relative magnitudes of the three correlation functions are different than in Figure 2. Furthermore, dynamical correlations due to impact–parameter averaging become important due to the non–negligible sideward directed flow, causing additional distortions at larger values of relative momenta (q > 40 MeV/c). The qualitative features of impact–parameter averaged correlation functions are therefore different from those for purely central collisions, making the extraction of a signal of toroidal (or disk–shaped) density distributions difficult, if not impossible. Nevertheless, BUU calculations predict correlation functions with shapes distinct from those representing emission from spherical sources of finite lifetime.

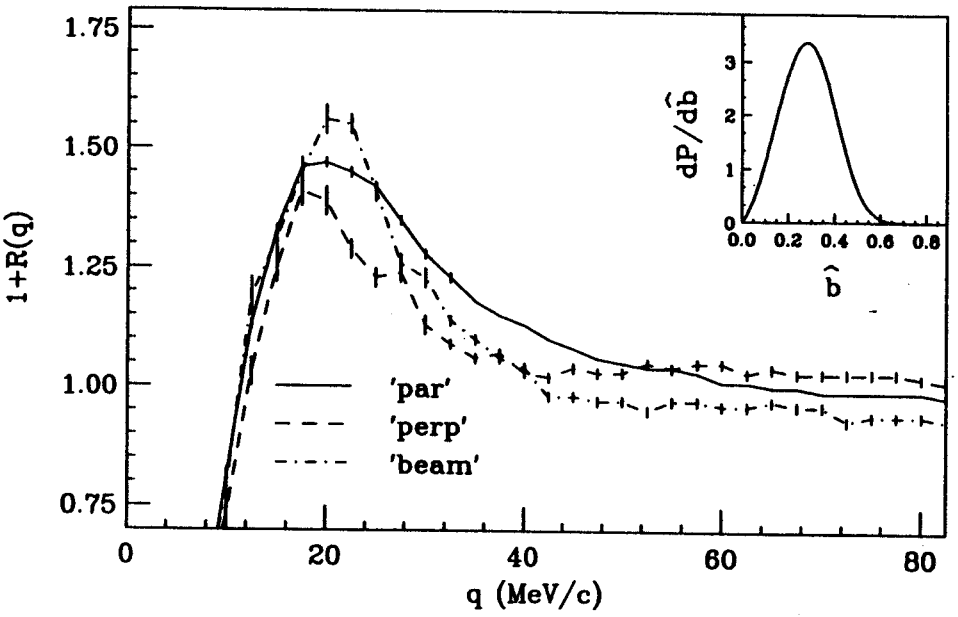

Figure 4: Two–proton correlation functions predicted by BUU transport calculations for central $^{36}Ar + ^{45}Sc$ collisions at E/A=80 MeV. The assumed distributions of impact parameter is shown in the insert.

Unfortunately, the statistical accuracy of our experimental data (References [6,9,10]) is not sufficient to allow such tests. Impact–parameter–selected correlation functions of improved statistical accuracy and with appropriately chosen directional cuts should, however, be able to test the nontrivial space–time evolution predicted by microscopic transport calculations. We believe, however, that such an experimental signature would be very difficult to interpret in a model–independent way.

References

1. L.G. Moretto, K. Tso, and G.J. Wozniak, Phys. Rev. Lett. **69**, 1884 (1992).
2. W. Bauer, G.F. Bertsch, and H. Schmaltz, Phys. Rev. Lett. **69**, 1888 (1992).
3. D.H.E. Gross, B.A. Li, and A.R. DeAngelis, Ann. Physik **1**, 467 (1992).
4. B. Borderie, B. Remaud, M.F. Rivet, and F. Sebille, Phys. Lett. B **302**, 53 (1985).
5. H.M. Xu, J.B. Natowitz, C.A. Gagliardi, R.E. Tribble, C.Y. Wong, and W.G. Lynch, Phys. Rev. C **48**, 933 (1993).
6. D.O. Handzy, M.A. Lisa, C.K. Gelbke, W. Bauer, F.C. Daffin, P. Dekowski, W.G. Gong, E. Gualtieri, S. Hannuschke, R. Lacey, T. Li, W.G. Lynch, C.M. Mader, G.F. Peaslee, T. Reposeur, S. Pratt, A.M. Vander Molen, G.D. Westfall, J. Yee, and S.J. Yennello, Phys. Rev. C **50**, 858 (1995).
7. L. Phair, W. Bauer, and C.K. Gelbke, Phys. Lett. B **314**, 271 (1993).
8. T. Glasmacher, C.K. Gelbke, and S. Pratt, Phys. Lett. B **314**, 265 (1993).
9. M.A. Lisa, C.K. Gelbke, W. Bauer, P. Dekowski, W.G. Gong, E. Gualtieri, S. Hannuschke, R. Lacey, T. Li, W.G. Lynch, C.M. Mader, G.F. Peaslee, T. Reposeur, S. Pratt, A.M. Vander Molen, G.D. Westfall, J. Yee, and S.J. Yennello, Phys, Rev. Lett **70**, 3709 (1993).
10. M.A. Lisa, C.K. Gelbke, W. Bauer, P. Dekowski, W.G. Gong, E. Gualtieri, S. Hannuschke, R. Lacey, T. Li, W.G. Lynch, C.M. Mader, G.F. Peaslee, T. Reposeur, S. Pratt, A.M. Vander Molen, G.D. Westfall, J. Yee, and S.J. Yennello, Phys, Rev. Lett **71**, 2863 (1993).
11. C.P. Montoya, W.G. Lynch, D.R. Bowman, G.F. Peaslee, N. Carlin, R.T. deSouza, C.K. Gelbke, W.G. Gong, Y.D. Kim, M.A. Lisa, L. Phair, M.B. Tsang, J. Webster, C. Williams, N. Colonna, K. Hanold, M.A. McMahan, G.J. Wozniak, and L.G. Moretto, Phys. Rev. Lett. **73**, 3070 (1994).

IMPACT PARAMETER DEPENDENCE OF THE DISAPPEARANCE OF TRANSVERSE FLOW IN NUCLEAR COLLISIONS

R. Pak, W. J. Llope[a], D. Craig[b], E. E. Gualtieri, S. A. Hannuschke,
R. A. Lacey[c], J. Lauret[c], A. C. Mignerey[d], D. E. Russ[d], N. T. B. Stone,
A. M. Vander Molen, G. D. Westfall, and J. Yee

The study of collective flow in nucleus-nucleus collisions can provide information about the nuclear equation of state (EOS) [1,2,3,4]. Collective transverse flow in the reaction plane disappears at an incident energy, termed the balance energy (E_{bal}) [5], where the attractive scattering dominant at energies around 10 MeV/nucleon balances the repulsive interactions dominant at energies around 400 MeV/nucleon [6,7,8,9,10,11,12,13,14]. We have recently completed a systematic study of the disappearance of flow for central collisions in symmetric entrance channels, which showed that E_{bal} scales as $A^{-1/3}$ where A is the mass of the combined projectile-target system [15]. The general trend of this result, which was reproduced by Boltzmann-Uehling-Uhlenbeck model [15] and Landau-Vlasov model [16] calculations at a fixed impact parameter, demonstrated that E_{bal} is insensitive to the compressibility of the EOS but sensitive to the in-medium nucleon-nucleon cross section.

The importance of the role of the impact parameter in the determination of the disappearance of flow has been recognized [7,10]. In symmetric collisions the compressed midrapidity participant volume is expected to decrease in size with increasing impact parameter, so that a larger incident energy is required to compensate for the effects of the mean field in more peripheral collisions. Using a transverse momentum analysis method [17], we show that flow can be determined from midrapidity participant fragments for relatively peripheral collisions. The impact parameter dependence of the balance energies extracted from the measured flow values agrees with predictions from Quantum Molecular Dynamics (QMD) model calculations.

The present measurements were carried out with the Michigan State University 4π Array [18] at the National Superconducting Cyclotron Laboratory (NSCL) using beams from the K1200 cyclotron. A target of 1.0 mg/cm^2 scandium was bombarded with ^{40}Ar projectiles ranging in energy between 35 and 115 MeV/nucleon in 10 MeV/nucleon steps. Prior to this experiment, the MSU 4π Array was upgraded with the High Rate Array (HRA). The HRA is a close-packed pentagonal configuration of 45 phoswich detectors spanning laboratory polar angles $\theta \approx 3°$ to $\approx 18°$. With the HRA we obtained Z resolution up to the charge of the ^{40}Ar projectile, and mass resolution for the hydrogen isotopes. The main ball of the 4π Array consists of 55 Bragg curve counters followed by 170 phoswich detectors covering the angles $\theta \approx 18°$ to $\approx 162°$. Data were taken with a minimum bias trigger that required at least one hit in the HRA (HRA-1 data), and a more central trigger where at least two hits in the main ball (Ball-2 data) were required. The flow analysis described below was performed with the Ball-2 data as done in Ref. [15].

We use a transverse momentum analysis method [17] in which the impact parameter and the orientation of the reaction plane must be determined. The impact parameter, b, of each event is assigned through cuts on centrality variables [19] measured with the improved acceptance of the upgraded 4π Array. Using methods similar to those detailed in Ref. [20], the reduced transverse kinetic energy, $\hat{E}_t$, is found to be an appropriate variable to use as a centrality filter for this system over the range of beam energies studied, and does not autocorrelate with the flow observables. The reaction plane is calculated using the method of azimuthal correlations [21], which is a good method to determine the reaction plane in cases where transverse collective motion can become weak (*e.g.* beam energies near the balance energy).

As an example of the method used for impact parameter selection, events with $\hat{E}_t$ in the top 10% of the inclusive $\hat{E}_t$ spectrum were assigned to the most central bin. This corresponds to a reduced impact parameter of $\hat{b} = (b/b_{max}) \leq 0.32$ as calculated through a simple geometric prescription [19], where b_{max} represents the largest impact parameter leading to a triggered event. In order to estimate b_{max} for the Ball-2 data, we adjusted the overall normalization of the inclusive $\hat{E}_t$ spectrum to fit the same distribution for data taken with the HRA-1 trigger. We extracted a value of $b_{max} = 0.88(R_{proj} + R_{targ})$, where $(R_{proj} + R_{targ})$ is the sum of the projectile and target radii, under the assumption that for the HRA-1 data $b_{max} = (R_{proj} + R_{targ})$. This results in a corrected $\hat{b} \leq 0.28$ for the top 10% most central events. The correction factor did not vary significantly over the range of beam energies we measured. The remaining impact parameter bins and the corresponding reduced impact parameters in the simple geometric picture are summarized in Table 1. Also listed in this table are the effective values of the reduced impact parameter corrected for bias due to the hardware trigger condition.

Bin No.	Cut on $\hat{E}_t$	Geometric $\hat{b}$	Corrected $\hat{b}$
BIN1	top 10%	0.31	0.28
BIN2	10% - 20%	0.45	0.39
BIN3	20% - 30%	0.55	0.48
BIN4	30% - 40%	0.63	0.56
BIN5	40% - 50%	0.71	0.62
BIN6	50% - 75%	0.87	0.76
BIN7	bottom 25%	1.00	0.88

Table 1: Reduced impact parameter bins. The values of $\hat{b}$ correspond to the upper limit of each bin.

In Fig. 1 we show the mean transverse momentum in the reaction plane, $\langle p_x \rangle$, plotted versus the normalized center-of-mass (CM) rapidity, $(y/y_{proj})_{CM}$. The data are for He fragments from 55 MeV/nucleon ^{40}Ar+^{45}Sc reactions at four different reduced impact parameter bins (as listed in Table 1). The errors shown in each panel are statistical. The data exhibit the characteristic "S-shape" associated with collective transverse flow in the reaction plane. The offsets from the origin occur because no recoil correction was applied in the reaction plane calculation for this analysis. We found that a constant fraction of the system mass could not be used in the recoil correction [9] to make the offsets vanish for all impact parameters at a given beam energy. The data are fit with a straight line in the midrapidity region $-0.5 \leq (y/y_{proj})_{CM} \leq 0.5$, and the slope of this line is defined as the transverse flow. As the impact parameter increases in Fig. 1, the transverse flow increases, passes through a maximum, and diminishes for the most peripheral impact parameter bin shown. This behavior is in qualitative agreement with previous results that range in beam energy from 55 MeV/nucleon [22] to 400 MeV/nucleon [2]. That collective transverse flow is maximal at some intermediate impact parameter is reasonable because it must vanish at the extrema, *i.e.* for grazing and perfectly central collisions.

The extracted values of the transverse flow plotted versus the beam energy are shown in Fig. 2 for the four most central reduced impact parameter bins (as listed in Table 1). The errors shown are the statistical errors on the slopes of the linear fits. The data points for each $\hat{b}$-bin are fit with a second-order polynomial for the purpose of finding the balance energy, E_{bal}. As in Ref. [5], we found that the analytic form of the fitting function does not significantly affect the value of the extracted balance energy. We assume collective transverse flow to be symmetric in the vicinity of the balance energy, and

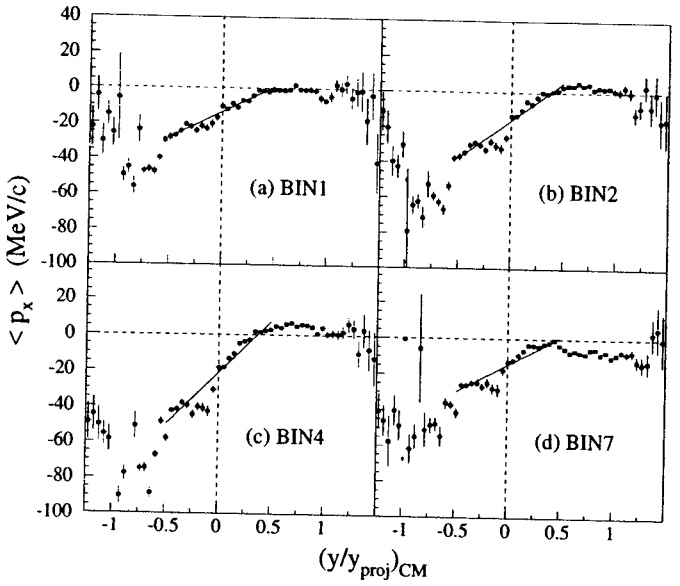

Figure 1: Mean transverse momentum in the reaction plane versus the normalized rapidity in the center-of-mass frame for $Z = 2$ fragments in 55 MeV/nucleon ^{40}Ar+^{45}Sc reactions. The reduced impact parameter bins, as indicated in each panel, are listed in Table 1. The straight lines are fit in the region -0.5 $\leq (y/y_{proj})_{CM} \leq$ 0.5.

our measurements are unable to distinguish the sign (+ or -) of the flow, so that a parabolic function is the lowest order symmetric fit we can use without *a priori* knowledge of E_{bal}. In addition this local parabolic fit, also investigated in Ref. [5], facilitates extraction of the balance energy for the larger impact parameters where the flow does not strongly reappear.

The curves shown in Fig. 2 pass through minima for which the value of the abscissa corresponds to the balance energy at each reduced impact parameter, $E_{bal}(b)$. Because no recoil correction was used in the reaction plane determination, the curves do not pass through zero at $E_{bal}(b)$, and this artifact of momentum conservation becomes larger for more peripheral collisions. For the largest $\hat{b}$-bin displayed only a lower limit on the value of $E_{bal}(b)$ could be determined from these data, because the higher beam energies necessary to extract $E_{bal}(b)$ for more peripheral collisions were not available from the K1200 cyclotron. The shift in the minima of the curves in Fig. 2 clearly indicates that $E_{bal}(b)$ increases as the impact parameter increases. This result is in qualitative agreement with Ref. [10], but here we are able to more definitively extract $E_{bal}(b)$ for larger impact parameters because our measurements include more data points above the balance energy.

Transport model calculations can incorporate soft and stiff descriptions of the nuclear EOS as well as momentum dependence in the mean field. Predictions of Quantum Molecular Dynamics (QMD) model [23] calculations are displayed in Fig. 3 for a stiff equation of state with momentum dependence (open circles) and without momentum dependence (open squares) for ^{40}Ca+^{40}Ca reactions. Also shown in this figure are the measured values of the balance energies for ^{40}Ar+^{45}Sc reactions extracted for the four most central reduced impact parameter bins (closed triangles). The errors on the measured values of the balance energies are statistical. We find that $E_{bal}(b)$ increases approximately linearly as a function of the impact parameter in agreement with Ref. [23]. The result shown for BIN2 ($\hat{b} = 0.39$) is comparable with our previous measurement of E_{bal} for ^{40}Ar+^{45}Sc of 87±12 MeV/nucleon for an uncorrected $\hat{b}$ = 0.40 assigned through a cut on the total transverse momentum [15]. Although additional work is needed to

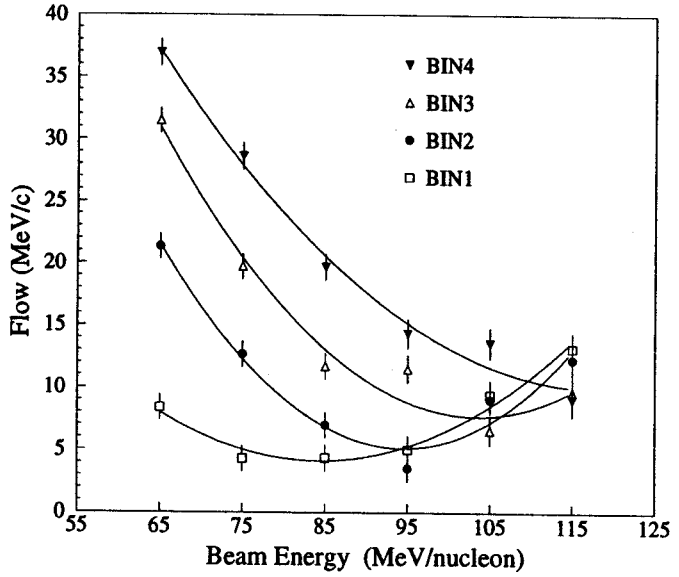

Figure 2: Excitation functions of the measured transverse flow in the reaction plane for $Z = 2$ fragments at four reduced impact parameter bins for ^{40}Ar+^{45}Sc reactions. The corresponding values of $\hat{b}$ are given in Table 1. The solid curves are parabolic fits as described in the text.

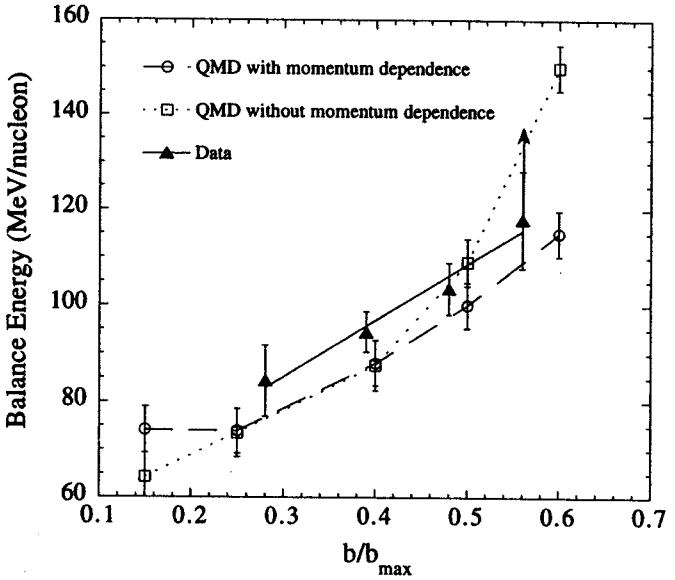

Figure 3: Measured balance energies for ^{40}Ar+^{45}Sc reactions at the four most central reduced impact parameter bins compared with the predictions of the QMD model with and without momentum dependence for ^{40}Ca+^{40}Ca reactions [23]. The curves are included only to guide the eye.

make a more definitive comparison between experiment and theory, the trends of the data suggest better agreement with the calculation incorporating momentum dependence in the mean field.

In summary, we have investigated the impact parameter dependence of the disappearance of transverse flow for ^{40}Ar+^{45}Sc reactions using the MSU 4π Array upgraded with the HRA. Our results indicate that the balance energy increases approximately linearly as a function of impact parameter. Physically this dependence could result from a smaller participant zone in more peripheral collisions, so that a larger incident energy is required to overcome effects of the mean field. Comparison of the trends in our measured values of $E_{bal}(b)$ is consistent with predictions of QMD model calculations. We agree with the point of view expressed in Ref. [23] that knowledge of the impact parameter is necessary before conclusions about the nuclear EOS can be drawn from the balance energy.

a. T.W. Bonner Nuclear Laboratory, Rice University, Houston, TX 77251.
b. Department of Physics, University of Wisconsin, Madison, WI 53706.
c. Department of Chemistry, SUNY - Stony Brook, Stony Brook, NY 11794.
d. Department of Chemistry, University of Maryland, College Park, MD 20742.

References

1. H. Stöcker and W. Greiner, Phys. Rep. 137, 277 (1986).
2. H.H. Gutbrod, A.M. Poskanzer, and H.G. Ritter, Rep. Prog. Phys. 52, 1267 (1989).
3. P. Danielewicz *et al.*, Phys. Rev. C 38, 120 (1988).
4. G. Peilert, H. Stöcker, and W. Greiner, Rep. Prog. Phys. 57, 533 (1994).
5. C.A. Ogilvie *et al.*, Phys. Rev. C 42, R10 (1990).
6. J.J. Molitoris and H. Stöcker, Phys. Lett. 162B, 47 (1985).
7. G.F. Bertsch, W.G. Lynch, and M.B. Tsang, Phys. Lett. B 189, 384 (1987).
8. D. Krofcheck *et al.*, Phys. Rev. Lett. 63, 2028 (1989).
9. C.A. Ogilvie *et al.*, Phys. Rev. C 40, 2592 (1989).
10. J.P. Sullivan *et al.*, Phys. Lett. B 249, 8 (1990).
11. W.M. Zhang *et al.*, Phys. Rev. C 42, R491 (1990).
12. D. Krofcheck *et al.*, Phys. Rev. C 43, 350 (1991).
13. W.Q. Shen *et al.*, Nucl. Phys. A551, 333 (1993).
14. J. Lauret *et al.*, Phys. Lett. B 339, 22 (1994).
15. G.D. Westfall *et al.*, Phys. Rev. Lett. 71, 1986 (1993).
16. V. de la Mota *et al.*, Phys. Rev. C 46, 677 (1992).
17. P. Danielewicz and G. Odyniec, Phys. Lett. 157B, 146 (1985).
18. G.D. Westfall *et al.*, Nucl. Inst. and Methods A238, 347 (1985).
19. C. Cavata *et al.*, Phys. Rev. C 42, 1760 (1990).
20. W.J. Llope *et al.*, Phys. Rev. C 51, 1325 (1995).
21. W.K. Wilson *et al.*, Phys. Rev. C 45, 738 (1992).
22. J. Péter, Nucl. Phys. A545, 173c (1992).
23. S. Soff *et al.*, Phys. Rev. C 51, 3320 (1995).

TIME SCALE FOR MULTIFRAGMENTATION IN INTERMEDIATE ENERGY HEAVY-ION REACTIONS

D. Fox[a], R. T. de Souza[b], T. Glasmacher, L. Phair[c], D. R. Bowman[a], N. Carlin[d], C. K. Gelbke, W. G. Gong[c], Y. D. Kim[e], M. A. Lisa[c], W. G. Lynch, G. F. Peaslee[f], M. B. Tsang, and F. Zhu[g]

To characterize the evolution of the spatial-temporal extent of the decaying system with increasing incident energy, we have measured an excitation function for the system ^{36}Ar+^{197}Au at E/A=50, 80, and 110 MeV. We have explored the dependence of IMF-IMF correlation functions on the spatial-temporal extent of the decaying system by comparing the measured correlation functions to model predictions covering a wide range of mean emission times and source size. We have also probed the effect on the correlation functions of additional charged particle emission. In this paper, we focus on central collisions ($b/b_{max} \leq 0.2$).

The experiment was performed using the K1200 cyclotron at MSU-NSCL. ^{36}Ar beams at E/A=50, 80, and 110 MeV, with an intensity of approximately 1x10^8 particles per second impinged on a ^{197}Au target with an areal density of 1 mg/cm^2. Charged particles emitted into the angular range $9° \leq \theta_{lab} \leq 160°$ were detected using the MSU Miniball array 2. The trigger condition required that at least two detectors in the Miniball were triggered in order to record an event.

The strength of the IMF-IMF final state interaction is dependent on the initial spatial-temporal separation of the two fragments. Fragments emitted from a source with a relatively short mean IMF emission time, τ, will, on average, experience a stronger final state interaction than fragments emitted from a source with a longer mean IMF emission time. Similarly, fragments which are emitted from a source with a small radius, R_S, will have a stronger final state interaction than fragments emitted from a source with a larger radius. The strength of the final-state interaction can be measured by using the two-IMF correlation function $R(v_{red})$ which is defined in terms of the ratio of the coincidence yield, Y_{12}, to the product of the single particle yields, Y_1 and Y_2.34. All correlation functions presented in this paper have been normalized to unity in the region $0.026c \leq v_{red} \leq 0.035c$.

We have used a 3-body Coulomb trajectory model to extract the spatial-temporal size of the emitting system and to investigate the effect of the emitting system on the IMF-IMF correlation functions. In the 3-body Coulomb trajectory calculation the decaying system, with initial charge, Z_S, initial mass number, A_S, and radius, R_S, emits the first IMF, with initial separation between source and IMF given by $R_S + R_{IMF}$, and then recoils. The trajectories of the emitted IMF and the source residue are calculated up to time t when the second IMF is emitted. The emission time t of the second IMF is assumed to be exponential with a mean time τ. The charge and energy of the two IMFs sample the measured Z-distributions and energy spectra. The mass number of each IMF is taken to be twice its atomic number.

Previously published comparisons between 3-body trajectory calculations and these data were restricted to only a few combinations of R_S and τ 5. In the present analysis, at each beam energy the calculations have been carried out for two different emitting source sizes, Z_S=40 and A_S=96, and Z_S=79 and A_S=197.

A clear minimum is seen in the χ^2/ν running along the diagonal between the R_S and τ axes; and, for a fixed source size, Z_S and A_S, the spatial-temporal extent of the emitting system decreases with increasing beam energy.

The behavior of τ as a function of R_S for the 3-body trajectory calculations is shown in Fig. 1(a).

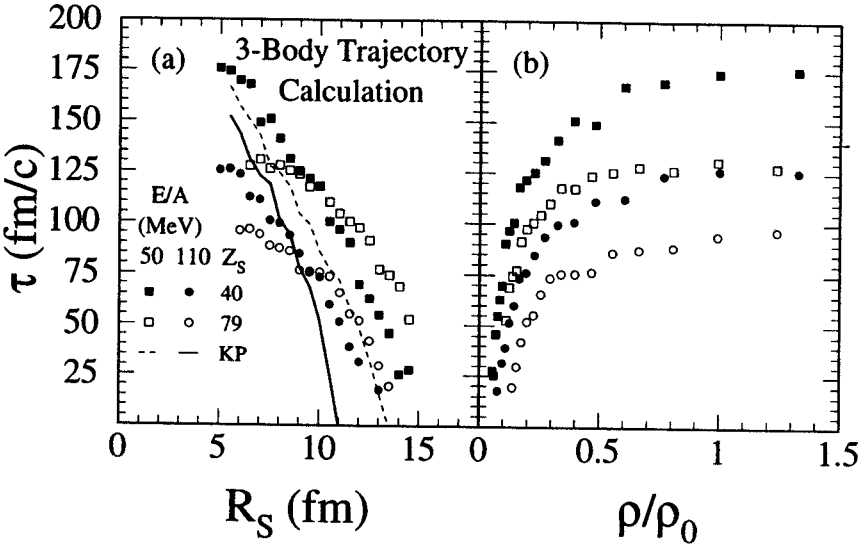

Figure 1: Mean emission times as a function of (a) R_S and (b) ρ/ρ_0 extracted from the data using a 3-body trajectory model. Extracted mean emission times for central ^{36}Ar+^{197}Au collisions at E/A=50 (squares) and 110 MeV (circles) are shown. The open symbols are for a source with initial Z_S=79 and A_S=197, the solid symbols are for a source with initial Z_S=40 and A_S=96. The lines are for Koonin-Pratt calculations.

The solid points are for the 3-body trajectory calculations carried out with Z_S=40 and A_S=96, the open points are for Z_S=79 and A_S=197, and the lines show the corresponding results from the Koonin-Pratt formalism. The 3-body trajectory calculations indicate a decrease in the spatial-temporal extent of the emitting system with increasing beam energy. Examining the effect of the two different initial choices of Z_S and A_S we see that for $R_S \leq 8$ fm the larger source results in the extraction of a shorter mean emission time, while for R_S >10 fm the larger source indicates a longer mean emission time. In Fig. 1(b) τ has been replotted in terms of the ratio of the density of the decaying system, ρ, to normal nuclear density, ρ_0. For all four cases shown in Fig. 1(b) the mean emission time initially rises steeply with increasing density until $\rho/\rho_0 \approx 0.3$. For $\rho/\rho_0 > 0.3$ the mean emission time is almost independent of the density of the emitting system. Furthermore, for a given density the calculation for the smaller initial source leads to a longer extracted mean emission time. It is interesting to note that many theoretical calculations require freeze out densities of $\approx 0.3\rho_0$. For $\rho/\rho_0 \approx 0.3$, the mean emission time for E/A=50 MeV is 115-135 fm/c. The mean emission time decreases with increasing beam energy to $\tau \approx$75-100 fm/c at E/A=110 MeV.

At the highest incident energy, E/A=110 MeV, an average of four IMFs and at least 28 light charged particles are detected in central collisions 6. Therefore, in order to study possible effects of the interaction all charged fragments on the correlations functions we have written a generalized N-body Coulomb trajectory code. In these calculations 8, we start with a heavy residue of charge Z_{res} located at the center of a sphere of radius R. The remainder of the initial charge, Z_{tot}=97, is then distributed as additional particles based on the measured Z-distribution. The particles are assigned random, non-overlapping positions within the sphere and are emitted simultaneously with an isotropic angular distribution in the center of mass. The masses of all particles are taken from the minimum in the valley of β-stability. The initial energy of each fragment is chosen to sample a Maxwell-Boltzman distribution with temperature T.

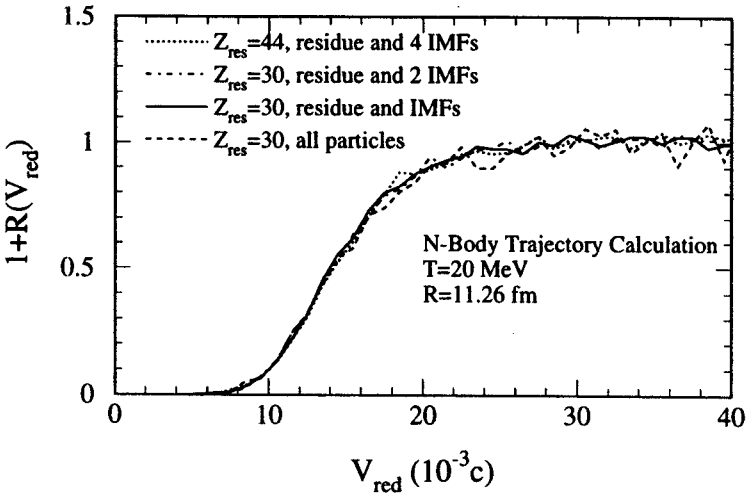

Figure 2: Results of N-body Coulomb trajectory calculations with T=20 MeV, R=11.26 fm. The dashed line is for the full calculation with Z_{res}=30 in which all charged particles are included, case (a). The other line types represent limited calculations in which only the residue and IMFs with $4 \leq Z \leq 9$ are included in the calculation. For the solid line fragments were formed using the measured Z distribution for all charges, but only those IMFs with $4 \leq Z \leq 9$ were then tracked along with a Z_{res}=30 residue, case (b). The dash-dotted line represents a calculation in which only two IMFs with $4 \leq Z \leq 9$ and the residue, with Z_{res}=30 were considered, case (c). The dotted line is for a calculation with Z_{res}=44 and four IMFs with $4 \leq Z \leq 9$, case (d).

The trajectories of all charged bodies are then calculated and the correlation function is constructed based upon the asymptotic momenta of the fragments after filtering for the detector acceptance.

The results of four different N-body calculations with T=20 MeV, R=11.26 fm are compared in Fig, 2. The four calculations are:

(a) A full N-body calculation in which the residue, Z_{res} = 30, and the equation of motion of all charged bodies are integrated, dashed line.

(b) All particles are generated, but the equations of motion are integrated only for the residue, Z_{res} = 30, and IMFs with $4 \leq Z \leq 9$, solid line.

(c) Only the residue, Z_{res} = 30, and two IMFs with $4 \leq Z \leq 9$ are generated and the equations of motion of all three particles are integrated, dash-dotted line.

(d) Only the residue, Z_{res} = 44, and four IMFs with $4 \leq Z \leq 9$ are generated and the equations of motion of all five particles are integrated, dotted line.

A value of Z_{res}=30 in the N-body Coulomb calculation is comparable to Z_S=40 for the 3-body Coulomb trajectory calculation because Z_S in the 3-body calculation is the charge of the emitting system prior to emission of the IMFs. For all four cases only IMFs with $4 \leq Z \leq 9$ are used to construct the correlation functions.

In Fig. 2 we see very little difference between the four cases described above.

The large number of charged particles, included in case (a) and neglected in the other cases has no effect on the correlation function. In addition only tracking two IMFs, case (c), instead of all the IMFs also has a negligible effect on the correlation functions. It can, therefore, be concluded that only the residue

and two IMFs need be considered, all other particles have a negligible effect on the correlation functions.

Differences between the 3-body and N-body Coulomb trajectory models complicate direct comparison of their results. In the 3-body model the IMFs are emitted from the surface of a sphere with an initial momentum away from the residue. In the N-body calculation all particles are emitted from within the volume of a sphere with no correlation between the position and momentum of the particle. Due to the difference between volume and surface emission a given radius in the N-body calculation corresponds to a smaller radius in the 3-body calculation.

In summary, the spatial-temporal extent of the emitting source for central ^{36}Ar+^{197}Au interactions has been shown to decrease with increasing beam energy. Calculations with a 3-body Coulomb trajectory model show that the extracted mean emission time rises steeply as a function of the assumed density of the emitting system until $\rho/\rho_0 \approx 0.3$. For higher densities the extracted mean emission time is essentially flat as a function of ρ. Assuming $\rho/\rho_0 \approx 0.3$ leads to mean emission times of 115-135 and 75-100 fm/c at E/A=50 and 110 MeV respectively from comparisons to 3-body Coulomb trajectory calculations and mean emission times of 75 and 25 fm/c at E/A= 50 and 110 MeV respectively from comparisons to the Koonin-Pratt model. Calculations with an N-body trajectory code indicates that light charged particles and additional IMFs have a negligible effect on the measured correlation functions.

a. Present address: Chalk River Laboratories, Chalk River, Ontario K0J 1J0, Canada.
b. Present address: Department of Chemistry and Indiana University Cyclotron Facility Indiana University, Bloomington, IN 47405
c. Present address: Lawrence Berkeley Laboratories, University of California, Berkeley, CA 94720.
d. Present address: Instituto de Fisica, Universidade de São Paulo, C. Postal 20516, CEP 01498, São Paulo, Brazil.
e. Present address: Physics Department, KEK 1-1 Oho, Tsukua, Ibaraki 305, Japan.
f. Present address: Physics Department, Hope College, Holland, MI 49423.
g. Present address: Brookhaven National Laboratory, Upton NY 11973.

References

1. D. Fox et al., Phys. Rev. C
2. R. T. de Souza et al., Nucl. Instr. and Meth. A295, 109 (1990).
3. Y. D. Kim et al., Phys.Rev.C45, 387 (1992).
4. Y. D. Kim, Phys.Rev.C45, 338 (1992).
5. D. Fox et al., Phys.Rev.C 47, R421 (1993).
6. R. T. de Souza et al., Phys. Lett. B268, 6 (1991).
7. L. Phair et al., Phys. Lett. B285, 10 (1992).
8. T. Glasmacher et al.,Phys. Lett. B314, 265 (1993).

COULOMB INSTABILITIES AND MULTIFRAGMENT DECAYS

M. D'Agostino[f], G. J. Kunde, P. M. Milazzo[f], J. D. Dinius, M. Bruno[f], N. Colonna[e], M. L. Fiandri[f], C. K. Gelbke, T. Glasmacher, F. Gramegna[g], D. O. Handzy, W. C. Hsi, M. Huang, M. A. Lisa[a], W. G. Lynch, P. F. Mastinu[f], C. P. Montoya[b], A. Moroni[h], G. F. Peaslee[c], L. Phair[a], R. Rui[i], C. Schwarz[d], M. B. Tsang, G. Vannini[i], and C. Williams

Big nuclear systems are fundamentally unstable due to the long range coulomb force. At low excitation energies such instabilities lead to fission decay in highly charged ($Z > 90$) nuclei [1]. Even more highly charged systems ($184 \geq Z \geq 92$) can be momentarily formed via central collisions between heavy nuclei. At energies near the Coulomb barrier, such collisions lead predominantly to binary final states [2]. In central collisions at incident energies of $E/A \approx 30$ MeV, however, transport model calculations [3] predict that Coulomb instabilities will drive very highly charged systems to bubble-like multifragment breakup configurations which subsequently disassemble via a slow Coulomb expansion. For very highly charged systems ($Z_{tot} \geq 130$) at low energies, few measurements of multifragment emission have been performed; at $E/A \approx 30$ MeV, for example, measurements suggest that bulk multifragmentation processes contribute little to a total reaction cross section dominated by strongly damped binary collisions 4, 5.

To investigate the role of Coulomb in the multifragment breakup, beams of Au ions at $E/A = 35$ MeV incident energy, accelerated by the K1200 cyclotron, were used to bombard Au foils of approximately 5 mg/cm^2 areal density. Light charged particles and intermediate mass fragments (IMF's: $3 \leq Z_{\rm IMF} \leq 20$) were detected at $23° \leq \Theta_{lab} \leq 160°$ by the MSU Miniball [6] and fragments with $3 \leq Z \leq 79$ at $3° \leq \Theta_{lab} \leq 23°$ by 44 gas-Si-Si(Li)-CsI detectors of the INFN Multics Array [7]. The charge identification thresholds were about 2, 3, and 4 MeV/nucleon in the Miniball for Z=3, 10, and 18, respectively, and about 1.5 MeV/nucleon in the Multics Array independent of fragment charge. The geometric acceptance of the combined array was greater than 87% of 4π.

The analysis focused upon central events with $N_c \geq 28$ corresponding to reduced impact parameter $\hat{b} \leq 0.1$ 8]. For such events, approximately 53% of the total charge is detected in the experimental apparatus, and a surprisingly large fraction, 58%, of this detected charge is bound in intermediate mass fragments IMF's, defined here by $3 \leq Z_{\rm IMF} \leq 20$. These IMF's are detected with an average multiplicity of $< N_{\rm IMF} > \approx 5.6$. Correcting for the efficiency of the detectors and multiplying this corrected multiplicity in the threshold–free region at rapidity $y \geq y_{\rm cm}$ by a factor of two, a mean IMF multiplicity $< N^{cor}_{\rm IMF} >= 10.8 \pm 1$ was determined. The corresponding efficiency corrected charge distribution, shown by the solid points in Fig. 1, is surprisingly flat. A similarly flat charge distribution, shown by the open points, is also observed for fragments emitted at center of mass angles of $\theta_{\rm cm} = 90° \pm 20°$ where one expects a reduced sensitivity to the decay of projectile- and target-like remnants. (Differences between the two sets of data are comparable to the systematic uncertainties in the efficiency correction.) For comparison, we show the charge distribution measured for central collisions at $E/A = 100$ MeV (solid squares) for the same system [9], and the charge distribution measured in peripheral collisions at $E/A = 1000$ MeV for the same system (open squares)[9]. Both of these charge distributions measured at higher energies decrease much more steeply with fragment charge.

Early investigations of high-energy hadron-nucleus collisions, revealed a power-law behavior, $p(A) \propto A^{-\tau}$, of the inclusive mass distributions [10], similar to that observed for the distributions of droplets for near-critical, macroscopic systems exhibiting a liquid and a gaseous phase [11]. Consistent

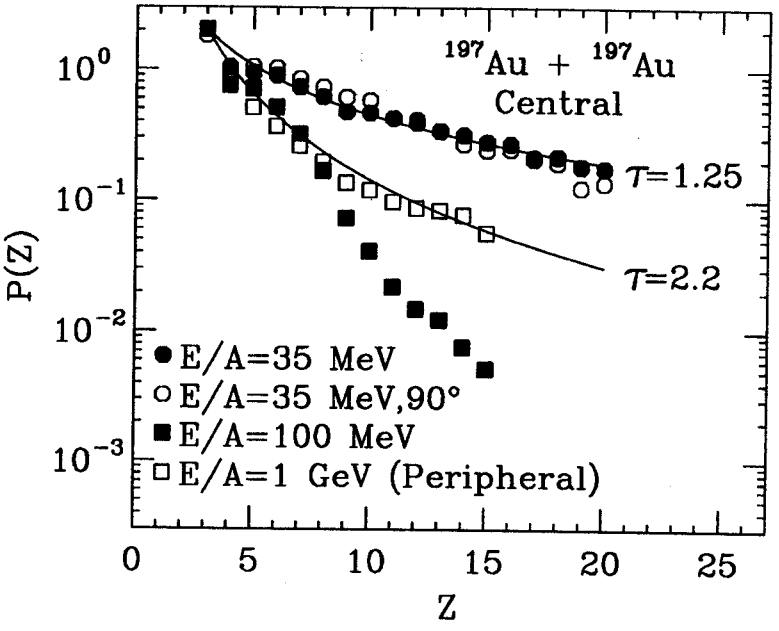

Figure 1: Efficiency corrected and angular integrated elemental probability distribution for fragments emitted in central collisions ($\hat{b} \leq 0.1$) for the reaction Au+Au at E/A = 35 MeV (solid points). The corresponding differential distribution at $\leq \Theta_{cm} = 90° \pm 20°$, normalized to the angular integrated data, is shown as open points. Elemental yields for central collisions at E/A = 100 MeV and peripheral collisions at E/A = 1000 MeV from ref. [9] are normalized to the lithium yield at E/A = 35 MeV and are shown by the solid and open squares respectively.

with this macroscopic analogy, values for the "critical parameter" of τ have been extracted [12, 13] from analyses of charge distributions measured for smaller systems containing 80-200 nucleons. After correction for finite size effects and detection efficiency values for $\tau \approx 2.2$ are obtained for peripheral collisions in the domain of limiting fragmentation; one such example is provided by the data for slowly expanding systems produced via peripheral collisions at E/A = 1000 MeV shown in Fig. 1. Similar data have been interpreted [12, 13, 14] as evidence for near critical behavior.

Such attempts to extract critical exponents [12, 13, 14] from scaling laws have relied heavily upon the assumption that the charge or mass distributions of systems at thermal equilibrium display minimum values for τ at the critical point. The charge distribution in Fig. 1 for E/A = 35 MeV is roughly consistent with $\tau \approx 1.25$, a value which is much smaller than the value $\tau \approx 2.2$ expected from scaling laws at the critical point of the liquid gas phase diagram. Compared to this difference, finite size corrections to τ, deduced from percolation model calculations for systems with $A \approx 400$ [13], are negligible. This prompts more detailed consideration of other factors that could enhance the production of heavier fragments.

Angular momentum [15, 16], Coulomb interactions [17, 18], non-equilibrium effects [19], and non-compact decay configurations [20] have been raised previously as important issues but have not been taken into account during the extraction [12, 13, 14] of critical exponents. In particular, the selection of events with impact parameters $\hat{b} \leq 0.1$ used in the construction of Fig. 1 could imply nonnegligible total angular momenta and possible contributions from strongly damped reactions, due to the finite resolution of the impact parameter filter. One may assess the importance of the statistical decay of rapidly rotating projectile- and target-like residues with enhanced branching ratios for fragment emission [15, 16, 21] by

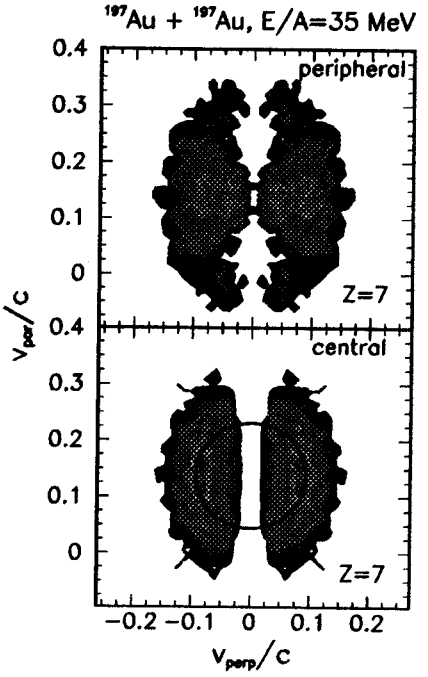

Figure 2: Velocity distribution for $Z = 7$ fragments for peripheral collisions ($\hat{b} \geq 0.7$, upper panel) and central collisions ($\hat{b} \leq 0.1$, lower panel). The circle indicates a *rms* velocity of v_{rms}=0.1c. (In this figure, the efficiency corrected velocity distributions at $y \geq y_{cm}$ have been reflected about $y = y_{cm}$ to obtain a thresholdless distribution for all values of y.)

examining the fragment velocity distributions, shown for Z=7 in Figure 2 for peripheral ($\hat{b} \geq 0.7$; upper panel) and central collisions ($\hat{b} \leq 0.1$; lower panel), respectively. Distributions for peripheral and central collisions both have a major component centered about mid-rapidity($y \approx y_{cm}$); ring-like emission patterns, centered about the projectile- and target-like residue velocities and characteristic of the statistical decay of projectile- and target-like residues, are only weakly observed. Consistent with previous observations [23], fragments are primarily formed in peripheral collisions by the fragmentation of a "neck" that momentarily connects projectile and target-like residues. This "neck" forms a "participant" source that grows in size and importance with decreasing impact parameter. The assumption of a constant *rms* fragment velocity of $v_{rms} = \left(< v_{cm}^2 >\right)^{1/2} = 0.1$c, extracted for fragments emitted in central collisions at $70° \leq \Theta_{cm} \leq 110°$ and shown as the circle in Fig. 2, approximates the participant source at other angles. Such a low value for v_{rms} is roughly consistent with the Coulomb disintegration of a single spherical source at a constant density of about $0.3\rho_0$.

While the statistical decay of equilibrated projectile- and target-like residues or of an equilibrated compound nucleus is unlikely for central collisions, it is possible, that for a phase space dominated decay mechanism, collective rotation could dictate large branching ratios for non-compound fragment emission [15, 16, 21]. Since such general considerations would also dictate the focusing of decay patterns into the plane perpendicular to the total angular momentum [21, 22], the importance of collective rotation can be tested by constructing $\alpha - \alpha$ azimuthal angular correlation functions $1 + R(\Delta\phi_{\alpha\alpha})$, defined by

$$\sum Y_{12}(\vec{p}_1, \vec{p}_2) = [1 + R(\Delta\phi_{\alpha\alpha})] \cdot \sum Y_1(\vec{p}_1) \cdot Y_2(\vec{p}_2) \,. \tag{1}$$

Here, $Y_{12}(\vec{p}_1, \vec{p}_2)$ is the coincidence yield, $Y_1(\vec{p}_1)$ and $Y_2(\vec{p}_2)$ are the singles yields for the particles 1 and

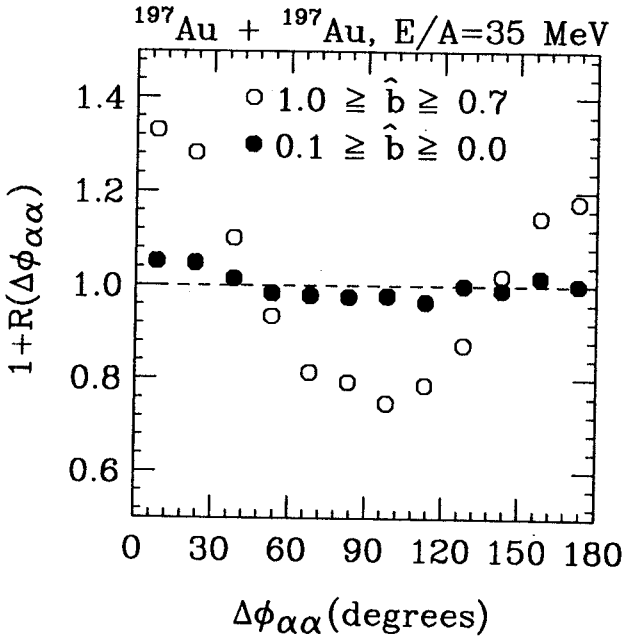

Figure 3: $\alpha - \alpha$ correlation functions [25] for peripheral (open points) and central (solid points) collisions. The relevant energy and angular gates are given in the text.

2 at momenta $\vec{p}_1$ and $\vec{p}_2$, and $\Delta\phi_{\alpha\alpha} = \phi_{\alpha_1} - \phi_{\alpha_2}$ is the relative azimuthal angle between the two alpha particles about the beam axis. Both sides of Eq. 2 are summed over momenta $\vec{p}_1$ and $\vec{p}_2$, for fixed $\Delta\phi_{\alpha\alpha}$. For systems rotating collectively, emission occurs preferentially at relative azimuthal angles of $\phi_{\alpha\alpha} = 0°$ and 180° corresponding to coplanar emission of the α particles in directions perpendicular to the total angular momentum.

Impact parameter selected correlation functions are shown in Figure 3 for an energy gate of $E_{\rm cm}/A \geq 7$MeV and an angular gate of $70° \leq \Theta_{\rm cm} \leq 110°$. Correlation functions for larger impact parameter collisions, $0.7 \leq \hat{b} \leq 1.0$, display large azimuthal anisotropies consistent with either a collective rotation of such residues or significant refractive "rotational" flow of nucleons along the surfaces of the combined system. In contrast, correlation functions of central collisions $\hat{b} \leq 0.1$ are nearly isotropic, indicating that anisotropies induced by rotational effects are comparatively negligible at such small impact parameters. No strong preference for the alignment of the angular momenta of the two alpha particles parallel to the total angular momentum is observed. This strongly suggests that the influence of rotation upon the fragment charge distributions will likewise be small.

There are a number of theoretical investigations that predict the observation of unusually flat fragment charge distributions. While the phase coexistence of highly charged liquid-gas phase mixtures has not been calculated at the critical density, the influence of the Coulomb interaction has been evaluated at lower densities within multiparticle phase space models [17, 18]. There, significantly larger fragment admixtures [17] and a preference for bubble-like decay configurations [18] have been observed in microcanonical calculations of the fragmentation of highly charged nuclear systems. Within bond percolation models [20], non-compact bubble-like decay configurations can result in reductions in the magnitude of the critical parameter τ by 20% relative to the decays of compact spherical systems. Classical

molecular dynamical simulations of the expansion and breakup of neutral, initially thermalized liquid drops predict a non-equilibrium fragmentation within the region of adiabatic instability [19, 24]. The resulting fragment - admixtures are significantly larger than those consistent with chemical equilibrium; compared to the equilibrium value $\tau \approx 2.3$ for the infinite system [19], effective critical exponents of $\tau_{eff} \approx 1.6$ are observed for expanding systems of 485 particles [19]. Observations of reduced values of the critical parameter $\tau \approx 1.7$ have also been attributed to the existence of a non-equilibrium mixture of fragments and a supersaturated nucleonic gas at freezeout [12]. Additional enhancements of *non-equilibrium* fragment emission due to Coulomb effects have only been partly addressed [24] and additional theoretical and experimental work is needed.

a. Present address: Nuclear Science Division, Lawrence Berkeley Laboratory, Univ. of California, Berkeley CA 94720, USA
b. Present address: Merrill Lynch, World Financial Center, North Tower, New York NY 10281, USA
c. Present address: Physics Department, Hope College, Holland MI 49423, USA
d. Present address: Gesellschaft für Schwerionenforschung, D-64220 Darmstadt, Germany
e. INFN, Via Amendola 173, 70126 Bari, Italy
f. Dipartimento di Fisica and INFN, Via Irnerio 46, 40126 Bologna, Italy
g. INFN, Laboratori Nazionali di Legnaro, Via Romea 4, 35020 Legnaro, Italy
h. INFN, Via Celoria 12, 20133 Milano, Italy
i. Dipartimento di Fisica and INFN, Via Valerio 2, 34127 Trieste, Italy

References

1. Robert Vandenbosch and John R. Huizenga, Nuclear Fission, Academic Press (1973) and ref. therein.
2. W.U. Schröder and J.R. Huizenga, Vol. 2 of Treatise on Heavy Ion Science, Plenum Press (1984) and refs. therein.
3. B. Borderie et al., Phys. Lett. B 302, 15 (1993).
4. J.F. Lecolley et al., Phys. Lett. B 325, 317 (1994).
5. B. M. Quednau et al., Phys. Lett. B 309, 10 (1993).
6. R.T. de Souza et al., Nucl. Instr. Meth. A 295, 109 (1990).
7. I.Iori et al., Nucl. Instr. Meth. A 325,458 (1993).
8. C. Cavata et al., Phys. Rev. C 42, 1760 (1990); Y.D. Kim et al, Phys. Rev. C 45, 338 (1992).
9. G.J. Kunde et al. Phys. Rev. Lett. 74, 38 (1995).
10. A.S. Hirsch et al., Phys. Rev. C 29, 508 (1984).
11. M.E.Fisher, Physics 3, 255 (1967).
12. M. Mahi et al., Phys. Rev. Lett. 60, 1936 (1988).
13. T. Li et al., Phys. Rev. Lett. 70, 1924 (1993).
14. M.L. Gilkes et al., Phys. Rev. Lett. 73, 590 (1994).
15. W.A. Friedman et al., Nucl. Phys. A471, 327c (1987).
16. L.G. Sobotka et at. Nucl. Phys. A471, 111c (1987).
17. D.H.E Gross et al., Nucl. Phys. A545, 187c (1992).
18. D.H.E Gross et al. Nucl. Phys. A567, 317 (1994).
19. S. Pratt et al., Phys. Lett. B 349, 261 (1995).
20. L. Phair et al., Phys. Lett. B 314, 271 (1995).
21. K. Sneppen et al., Nucl. Phys. A480, 342 (1988).
22. T.E.O. Erikson et al., Nucl. Phys. 8, 284 (1958); Nucl. Phys. 9, 689 (1959).
23. C.P. Montoya et al. Phys. Rev. Lett. 73, 3070 (1994).
24. A.Vincentini et at., Phys. Rev. C 31, 1783 (1985); R.J. Lenk et al. Phys. Rev. C 34, 172 1986); T.J. Schlagel et al. Phys. Rev. C 36, 162 (1986).
25. Rotational effects are responsible for the suppression of emission at $\Delta\phi \approx 90°$. Differences between the value of the $\alpha - \alpha$ correlation function at $\Delta\phi \approx 0°$ and 180° result from final state interactions between α-particles [26].
26. J.Pochodzalla et al. Phys. Lett. B 161,275 (1985)].

FRAGMENT FLOW AND THE MULTIFRAGMENTATION PHASE SPACE

G.J. Kunde, W.C. Hsi, W.D. Kunze,[g] A. Schüttauf,[g] A. Wörner,[f] M. Begemann-Blaich,[f] Th. Blaich,[h] D.R. Bowman,[a] R.J. Charity,[i] A. Cosmo,[j] A. Ferrero,[kb] C.K. Gelbke, J. Hubele,[f] G. Immé,[l] I. Iori,[k] P. Kreutz,[g] V. Lindenstruth,[f] M.A. Lisa,[c] W.G. Lynch, U. Lynen,[f] M. Mang,[g] T. Möhlenkamp,[m] A. Moroni,[k] W.F.J. Müller,[f] M. Neumann,[g] B. Ocker,[g] C.A. Ogilvie,[fd] G.F. Peaslee,[e] J. Pochodzalla,[f] G. Raciti,[l] T. Rubehn,[f] H. Sann,[f] W. Seidel,[m] V. Serfling,[g] L.G. Sobotka,[i] J. Stroth,[f] L. Stuttge,[j] S. Tomasevic,[j] W. Trautmann,[f] M.B. Tsang, A. Tucholski,[n] G. Verde,[l] C.W. Williams,[g] E. Zude,[f] and B. Zwieglinski[n]

The maximum multiplicity of intermediate mass fragments (IMFs) produced in central collisions between two heavy nuclei is observed at beam energies of about 100 MeV per nucleon [1, 2, 3]. At higher incident energies the multifragment breakup occurs predominantly at peripheral collisions [4, 5]. There the observed radial motion of fragments in peripheral collisions can be ascribed to the Coulomb repulsion between the produced particles [6] and the collective expansion velocities of the decaying spectator nuclei are small. Large collective velocities [7, 8, 9, 23], however, are observed in central collisions and the collective expansion is expected to have a strong influence on the fragment formation process [11, 12, 13, 14, 15, 16, 17].

To investigate the effect of expansion on fragment formation ^{197}Au targets with an areal density of 5 and 500 mg/cm^2 were bombarded with ^{197}Au ions of E/A=100 and 1000 MeV, respectively at the SIS heavy ion synchrotron of the GSI facility. The experiment at E/A=1000 MeV was performed with the ALADIN forward spectrometer system [18] which allowed efficient detection and identification of projectile fragments with Z$\geq$2. At the lower energy, fragment detection with close to 4π coverage was achieved by combining the ALADIN forward spectrometer with the MSU-MINIBALL/WU-MINIWALL array. The array allowed identification of the detected fragments by their element number for laboratory energies per nucleon between threshold energies of $E_{th}/A \approx$ 1.5 MeV (2.5 MeV) and punch-through energies for the MINIBALL of $E_{pu}/A \approx$ 80 (200 MeV) for Z=2 (Z=10) particles, respectively. Particles emitted to angles between the MINIBALL/WALL and the ALADIN magnet were detected in a 84 element Si-CsI(Tl) hodoscope.

The upper part of Fig. 1 shows the mean observed number of IMFs ($3 \leq Z_{IMF} \leq 30$) as a function of the reduced impact parameter $\hat{b}$. The impact parameter scale was derived from the multiplicity of light particles at E/A= 100 MeV [3] and Z_{bound} at E/A=1000 MeV [19]. At E/A =100 MeV a maximum mean fragment multiplicity of $\langle N_{IMF} \rangle \approx 10$ is detected in central collisions [3]. The majority of the fragments originate from the interaction region. At E/A = 1000 MeV, the maximum mean multiplicity of $\langle N_{IMF} \rangle \approx 5$ is seen in peripheral collisions. In this case, the projectile spectator is the dominant source of the IMFs. Correcting these numbers for the detection efficiency we find that in both cases the maximum IMF multiplicity normalized to the size of the decaying system is close to one IMF per 30 nucleons [20].

The element distribution of fragments produced in collisions corresponding to the maximum mean IMF multiplicity are compared in the lower part of Fig. 1. Consistent with previous investigations of Au+Au collisions [2] an exponential charge distribution is observed in central reactions. Although the size of the fragmenting system is smaller at E/A=1000 MeV, more heavy clusters are produced in peripheral multifragmentation and the Z-distribution shows a power-law behaviour. In the following, we will relate this striking difference to the difference in the collective expansion velocity.

Generally, the fragment momenta $\vec{p}$ may be decomposed into a random, "thermal" part $\vec{p}_{thermal}$, a

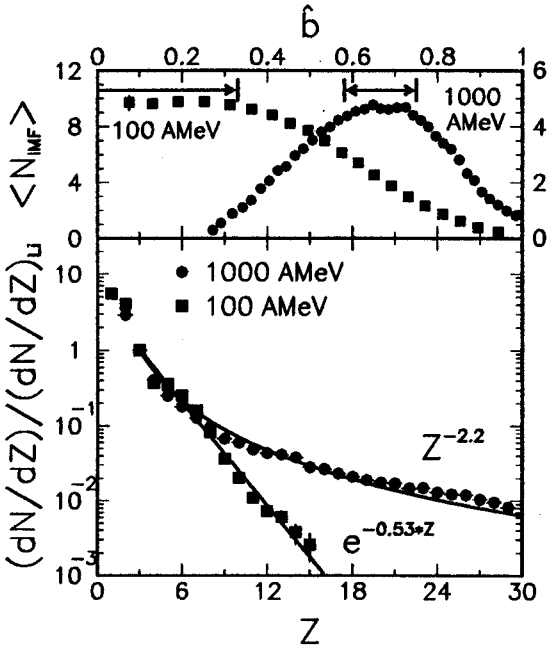

Figure 1: Top Part: Mean multiplicity of detected IMFs with $3 \leq Z \leq 30$ produced in Au+Au collisions at E/A=100 (left scale) and 1000 MeV (right scale) as a function of the reconstructed impact parameter $\hat{b}$. The lower part shows the charge distributions observed in the impact parameter range of maximum mean IMF multiplicity (indicated by the arrows in the upper part of the figure). The lines represent an exponential and power-law fit to the Z-distributions.

collective flow contribution $\vec{p}_{flow}$ and a momentum provided by the Coulomb repulsion $\vec{p}_{Coulomb}$. In the discussion below we assume a random component which is independent of the position $\vec{r}$ with respect to the center of the decaying system and an ordered velocity which is proportional to $|\vec{r}|$ [21, 22]. In this case, cross-terms between the collective and random component vanish on the average and the total mean kinetic energy $\langle E \rangle$ may be written as $\langle E \rangle = \langle E_{thermal} \rangle + \langle E_F \rangle$ where $\langle E_F \rangle$ reflects the sum of the initial expansive flow and the Coulomb induced motion.

The analysis of central collisions ($\hat{b} \leq 0.33$) at E/A=100 MeV shows mean kinetic energies per nucleon measured at Θ_{cm}=90°±10° of 16.2 MeV to 10.8 MeV for the charges 2 and 6 respectively [23, 20]. The upper limit for average kinetic energies of these fragments in peripheral collisions at E/A=1000 MeV is only 8.9 MeV to 4.4 MeV, respectively [5, 20]. Whereas it can be shown that the random (thermal) kinetic energies per nucleon are comparable for the two incident energies the two systems differ substantially with regard to the magnitude of collective expansion velocities [20].

A difference in collective velocities will lead to a different mass distribution, which will here be demonstrated in a coalescence picture. In order to provide simple analytic relations, we consider a self similar flow profile superimposed on a spherical, homogeneous, thermally decaying system. For simplicity, the density in momentum space is assumed to be proportional to p_{rms}^{-3}, where p_{rms} denotes the rms - momentum of the nucleons at freeze-out. The probability that a fragment of mass number A is formed in

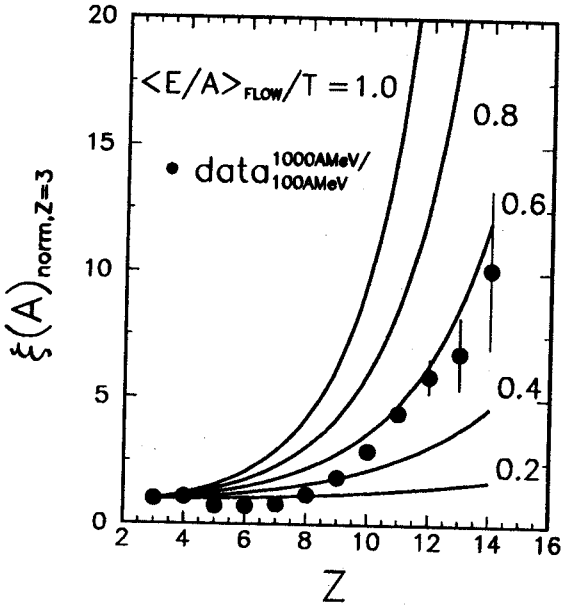

Figure 2: Suppression of heavy IMFs due to an expansive flow. The dots represent the ratio between the charge distributions measured at E/A=1000 MeV and 100 MeV (c.f. bottom part of Fig. 1). The full lines are results of a simple (analytic) coalescence model which considers the reduction of the density in momentum space due to a radial flow.

collisions which exhibit a flow is then reduced by the factor

$$f_A = \left[p_{rms}^{thermal} / \sqrt{(p_{rms}^{thermal})^2 + (p_{rms}^{flow})^2} \right]^{3 \cdot A} \tag{1}$$

in comparison to a situation without flow but the same freeze-out temperature.

In order to compare systems of different mass A_S, we furthermore apply a correction due to the variation of accessible volume with fragment mass as outlined in ref. [24] and obtain a total reduction factor

$$f(A_S, \langle E/A \rangle_{flow}/T) = \frac{\left(1 - \left(\frac{A_F}{A_S}\right)^{1/3}\right)^3}{\left(1 + \frac{2}{3}\frac{\langle E/A \rangle_{flow}}{T}\left(\frac{A_F}{A_S}\right)^{2/3}\right)^{3A/2}} . \tag{2}$$

Here, $\langle E/A \rangle_{flow}$ is the mean flow energy per nucleon, A_F is the fragment mass and T is the breakup temperature of the system. The total reduction factor depends only on the total mass of the system, A_S, and the ratio $\langle E/A \rangle_{flow}/T$.

The observed ratio between the two distributions shown in Fig. 1 - normalized at Z=3 - is given in Fig. 2 by the dots. The lines in Fig. 2 show the ratio $\xi(A_F)$ which compares a system of 150 nucleons having no initial flow (representative for the situation at E/A=1000 MeV) and a system composed of 320

nucleons with a flow ($\langle E/A \rangle_{flow}/T$) (representing central Au+Au collisions at E/A = 100 MeV). The curves have been normalized at A_F=6 and plotted assuming A=2·Z.

Our schematic coalescence model demonstrates that fragment formation may not only depend on the (local) temperature and density, but that it can be strongly affected by nonuniform collective velocity components. Thus, in the presence of a rapid collective expansion, static statistical models must be modified to incorporate such effects. The calculations indicate that the formation probability of heavy fragments is especially sensitive to the underlying flow dynamics. A satisfactory description of the measured intensity ratios of these heavy fragments is obtained for a value $\langle E/A \rangle_{flow}$/T=0.5-0.6.

a. Present Address: Chalk River Laboratories, Chalk River, Ontario K0J 1J0, Canada.
b. On leave from the Comision Nacional Energia Atomica, Argentina.
c. Present address: Nuclear Science Division, Lawrence Berkeley Laboratory, Univ. of California, Berkeley CA 94720, USA.
d. Present address: Department of Physics, MIT, Cambridge, MA 02139.
e. Present address: Physics Department, Hope College, Holland MI 49423, USA.
f. Gesellschaft für Schwerionenforschung, 64220 Darmstadt, Germany.
g. Institut für Kernphysik, Universität Frankfurt, 60486 Frankfurt, Germany.
h. Institut für Kernchemie, Universität Mainz, 55099 Mainz, Germany.
i. Department of Chemistry, Washington University, St. Louis, MO 63130, USA.
j. Centre de Recherches Nucléaires, 67037 Strasbourg, France
k. Dipartimento di Fisica, Universitá di Milano and I.N.F.N., 20133 Milano, Italy.
l. Dipartimento di Fisica dell' Universitá and I.N.F.N., 95129 Catania, Italy.
m. Forschungszentrum Rossendorf, 01314 Dresden, Germany.
n. Soltan Institute for Nuclear Studies, 00-681 Warsaw, Hoza 69, Poland.

References

1. See e.g. W. Bauer *et al.*, Nucl. Phys. A553, 749c (1993).
2. C. Kuhn *et al.*, Phys. Rev. C 48, 1232 (1993).
3. M.B. Tsang *et al.*, Phys. Rev. Lett. 71, 1502 (1993).
4. C.A. Ogilvie *et al.*, Phys. Rev. Lett. 67, 1214 (1991).
5. J. Hubele *et al.*, Phys. Rev. C 46, R1577 (1992).
6. V. Lindenstruth, PhD thesis (University Frankfurt) 1993, GSI-report GSI-93-18.
7. H.W. Barz *et al.*, Nucl. Phys. A531, 453 (1991).
8. W. Bauer *et al.*, Phys. Rev. C47, R1383 (1993).
9. S.C. Jeong *et al.*, Phys. Rev. Lett. 72, 3468 (1994).
10. W.C. Hsi *et al.*, preprint MSUCL-930, 1994.
11. D.E. Grady, J. Appl. Phys. 53, 322 (1982).
12. B.L. Holian and D.E. Grady, Phys. Rev. Lett. 60, 1355 (1988).
13. J. Desbois, R. Boisgard, C. Ngô, and J. Nemeth, Z. Phys. A 328, 101 (1987).
14. L. De Paula *et al.*, Phys. Lett. B258, 251 (1991).
15. W.A. Friedman, Phys. Rev. Lett. 60, 2125 (1988).
16. R. Donangelo, A. Romanelli, H. Schulz, and A.C. Sicardi-Schifino, Phys. Rev. C 49, 3182 (1994).
17. M. Colonna, M. DiToro, and A. Guarnera, LNS preprint (1994).
18. ALADIN Collaboration, U. Lynen *et al.*, GSI Report No. GSI-02-89 (unpublished).
19. J. Hubele *et al.*, Z. Phys. 340, 263 (1991).
20. G.J. Kunde et al. Phys. Rev. Lett. 74, 38 (1995).
21. J.P. Bondorf, S.I.A. Garpman, and J. Zimanyi, Nucl. Phys. A296, 320 (1978).
22. L.P. Csernai and H.W. Barz, Z. Phys. A 296, 173 (1980).
23. W.C. Hsi *et al.*, Phys. Rev. Lett. 73, 3367 (1994).
24. R. Donangelo and H.D. Marta, Phys. Rev. C 46, 805 (1992).

TWO- AND THREE-FRAGMENT REDUCED VELOCITY CORRELATION FUNCTIONS FOR CENTRAL $^{36}Ar+^{197}Au$ REACTIONS

T. Glasmacher, L. Phair[a], D.R. Bowman[b], C.K. Gelbke, W.G. Gong[a], Y.D. Kim[d], M.A. Lisa[a], W.G. Lynch, G.F. Peaslee[e], R.T. de Souza[c], M.B. Tsang, and F. Zhu[f]

The emission of intermediate mass fragments (IMF) has been established as a decay mechnism of excited nuclear matter formed in intermediate-energy heavy-ion collisions [1]. Certain statistical descriptions of these multifragment disintegrations are based upon the assumption of a sequential decay mechanism from a hot nuclear system undergoing equilibration between the individual disintegration steps [2]. Other models assume a nearly instantaneous fragmentation of an excited nuclear system at low density [3]. To distinguish between these two extreme scenarios, observables are being sought which can provide more detailed information about the space-time configuration of multifragmenting systems.

Two-fragment correlation functions at small relative velocities are sensitive to source dimensions and emission time scales [4], but existing data could often be reproduced by trading larger source dimensions for shorter emission time scales. This space-time ambiguity may be reduced by applying additional cuts on the relative angle between the relative velocity of the fragment pair and the velocity of its center-of-mass [5]. Recent calculations with a microcanonical model have shown that three (or more) fragment-correlation functions should produce a larger "Coulomb-hole" at small relative velocities than two-fragment correlation functions [6]. To explore the question whether or not three fragment correlation functions (also) contain additional information about the space-time characteristics of the multifragmenting system compared to two-fragment correlation functions we explore correlations between two and three fragments for central $^{36}Ar+^{197}Au$ collisions at E/A = 50 MeV.

The experiment was performed at the National Superconducting Cyclotron Laboratory at Michigan State University with the MSU Miniball phoswich detector array [7] and details of the experimental setup have been described previously [5,8].

As was done in ref. [5] we analyze reduced-velocity correlations between intermediate mass fragments ($4 \le Z_{IMF} \le 9$) detected in an angular range of $9° \le \theta_{lab} \le 40°$. Central collisions were selected by a cut on charged-particle multiplicity, $N_C \ge 19$. This centrality cut corresponds to a reduced impact parameter [8] of $b/b_{max} \le 0.3$ and less than 10% of the reaction cross section.

Following the notation of ref. [6], we define a correlation function of order w as

$$1+R(\Psi_\omega)=C\frac{N_{cor}(\Psi_\omega)}{N_{uncor}(\Psi_\omega)} \qquad (1)$$

Here, $N_{cor}(Y_W)$ is the observed Y_W distribution for fragments observed in the same event and $N_{uncor}(Y_W)$ is the Y_W distribution constructed from mixed events. (Specifically, we mixed fragment yields from the previous five events with fragment multiplicity w.) In Eq. 1, Y_W denotes the geometric mean of all reduced velocities $(v_{red})_{ij}$ between distinct pairs of fragments ij. For the particular case of two- and three-fragment correlation functions we have

$$\Psi_2=(v_{red})_{12} \text{ and } \Psi_3=\left(\prod_{ij=12,23,13}(v_{red})_{ij}\right)^{1/3}, \qquad (2)$$

where the reduced velocity $(v_{red})_{ij}$ is defined as [23,24]

$$(v_{red})_{ij} = \frac{(v_{rel})_{ij}}{\sqrt{Z_i + Z_j}} = \frac{p_i/m_i - p_j/m_j}{\sqrt{Z_i + Z_j}} \qquad (3)$$

Here the charge, mass and momentum of a fragment i are denoted by Z_i, m_i, and $\mathbf{p}_i$, respectively. The constant C in eq. 1 was chosen such that the correlation functions are normalized to unity for large reduced velocities ($0.035\ c \le v_{red} \le 0.05c$).

In order to deduce source parameters, we performed many-body Coulomb trajectory calculations as detailed in ref. [5].

Figure 1 summarizes the space-time ambiguity reported previously [5]. The solid points show the experimental two-fragment reduced-velocity correlation function. These correlations functions can be reproduced equally well by assuming fragment emission from a relatively large and short-lived source (R_S=10 fm and t=10 fm/c) or from a smaller, but longer-lived source (R_S= 8 fm and t=50 fm/c, or R_S= 5.5 fm and t=100 fm/c). As demonstrated in ref. [5], this ambiguity can be reduced by selective cuts on the orientation of the reduced velocity vector.

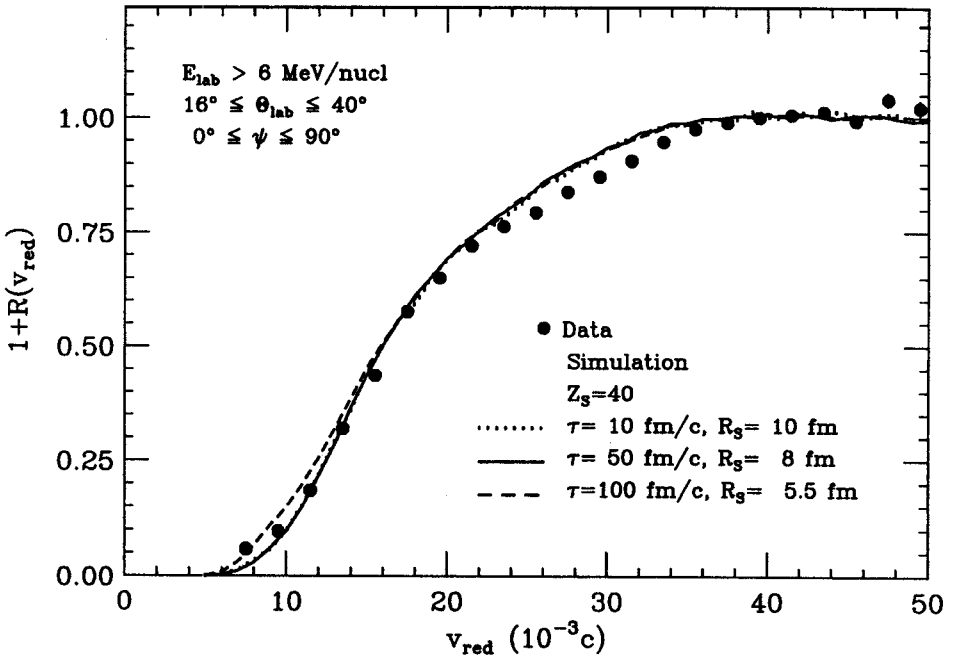

Figure 1. Measured (solid points) and simulated (curves) fragment-fragment correlation functions for intermediate mass fragments ($4 \le Z_{IMF} \le 9$) emitted in central ($b/b_{max} \le 0.3$) $^{36}Ar + ^{197}Au$ collisions at E/A = 50 MeV. The source parameters (radius R_S, charge Z_S and lifetime t, see [5]) are given in the figure and experimental error bars are indicated only when they are larger than the size of the plotted symbol. The simulated correlation functions are virtually indistinguishable.

Figure 2 compares the predicted three-fragment correlation functions to the experimental data. While the Coulomb-hole for the three-fragment correlation functions is indeed wider, the calculations -- performed with the same initial conditions as those shown in Fig. 1 -- provide a satisfactory description of the measured three-fragment correlation function. The space-time ambiguity is not reduced by the construction of the three-fragment correlation function, i.e. the previously noted ambiguity between radius and lifetime remains. Our study shows that for the present reaction two- and three-fragment reduced velocity correlation functions appear to contain more or less the same information about the emitting source.

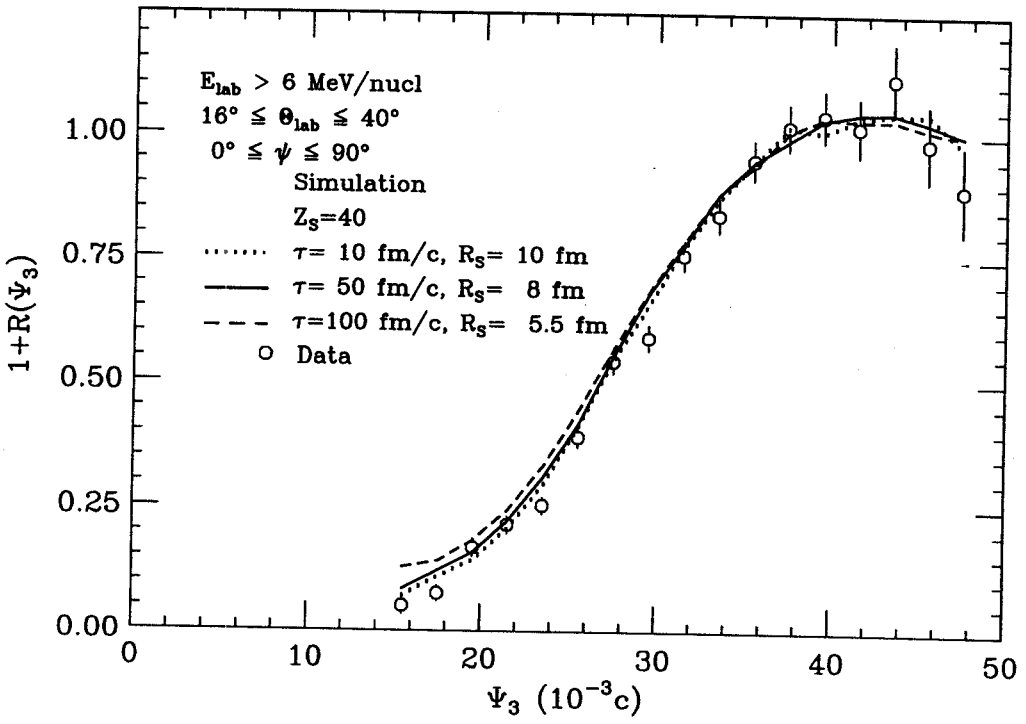

Figure 2. Measured (open points) and simulated (curves) three-fragment correlation functions. The source parameters are given in the figure and are identical to those used for the calculations shown in Fig. 1.

a. Present address: Lawrence Berkeley Laboratory, Berkeley, CA 94720, USA.
b. Present address: Chalk River Laboratories, Chalk River, Ontario K0J 1J0, Canada.
c. Present address: Indiana University Cyclotron Facility, Bloomington, IN 47405.
d. Present address: Physics Department, KEK 1-1 Oho, Tsukua, Ibaraki 305, Japan.
e. Present address: Physics Department, Hope College, Holland, MI 49423.
f. Present address: Brookhaven National Laboratory, Upton NY 11973.

References

1. Y.D. Kim et al., Phys. Rev. Lett. **63**, 494 (1989); Y. Blumenfeld et al., Phys. Rev. Lett. **66**, 576 (1991); E. Piasecki et al., Phys. Rev. Lett. **66**, 1291 (1991); D.R. Bowman et al., Phys. Rev. Lett. **67**, 1527 (1991); R.T. de Souza et al., Phys. Lett. **B268**, 6 (1991); K. Hagel et al., Phys. Rev. Lett. **68**, 2141 (1992); B. Lott et al., Phys. Rev. Lett. **68**, 3141 (1992); T.C. Sangster et al., Phys. Rev. **C46**, 1404 (1992); D.R. Bowman et al., Phys. Rev. **C46**, 1834 (1992); J.W. Harris et al., Nucl. Phys. **A471**, 241c (1987); C.A. Ogilvie et al., Phys. Rev. Lett. **67**, 1214 (1991); J.P. Alard et al., Phys. Rev. Lett. **69**, 889 (1992); M.B. Tsang et al., Phys. Rev. Lett. **71**, 1502 (1993); G.F. Peaslee et al., Phys. Rev. **C49**, R2271 (1994).
2. W. A. Friedman and W. G. Lynch, Phys. Rev. C **28**, 16 (1983); W. A. Friedman, Phys. Rev. Lett. **60**, 2125 (1988).
3. J. Bondorf, R. Donangelo, I. Mishustin, and H. Schulz, Nucl. Phys. A **444**, 460 (1985); D. Gross, Z. Xiao-ze, and X. Shu-yan, Phys. Rev. Lett. **56**, 1544 (1986).
4. R. Trockel et al., Phys. Rev. Lett. **59**, 2844 (1987); R. Bougault et al., Phys. Lett. **B232**, 291 (1989); Y.D. Kim et al., Phys. Rev. Lett. **67**, 14 (1991); Y.D. Kim et al., Phys. Rev. **C45**, 387 (1992); D. Fox et al., Phys. Rev. **C47**, R421 (1993); E. Bauge et al., Phys. Rev. Lett. **70**, 3705 (1993); T.C. Sangster et al., Phys. Rev. **C47**, R2457 (1993); D.R. Bowman et al., Phys. Rev. Lett. **70**, 3534 (1993); T. Ethvignot et al., Phys. Rev. **C48**, 618 (1993).; B. Kämpfer et al., Phys. Rev. **C48**, R955 (1993); O. Schapiro, A.R. De

Angelis and D.H.E. Gross, Nucl. Phys. **A568,** 333 (1994); O. Schapiro and D.H.E. Gross, Nucl. Phys. **A573**,143 (1994).
5. T. Glasmacher et al., Phys. Rev. **C50**, 952 (1994).
6. J. Lauret and R.A. Lacey, Phys. Lett. **B327,** 195 (1994).
7.R.T. de Souza et al., Nucl. Instr. Meth. **295**, 109 (1990).
8. L. Phair, *Multifragment Emission in Central Collisions of 36Ar + 197Au at E/A = 50, 80 and 110 MeV* (Ph.D. Thesis, Michigan State University, 1993).